

The Effect of Internally Generated Inner-Core Asymmetries on Tropical Cyclone Potential Intensity*

BO YANG, YUQING WANG, AND BIN WANG

International Pacific Research Center, and Department of Meteorology, School of Ocean and Earth Science and Technology, University of Hawaii at Manoa, Honolulu, Hawaii

(Manuscript received 8 December 2005, in final form 8 December 2006)

ABSTRACT

In a quiescent environment on an f plane, the internal dynamic processes of a tropical cyclone (TC) can generate axially asymmetric circulations (asymmetries) in its inner-core region. The present study investigates how these inner-core asymmetries affect TC intensity. For this purpose, a three-dimensional (3D) TC model and its axisymmetric (2D) version were used. Both have identical model vertical structure and use the same set of parameters and the same initial conditions. The differences between the two model runs are considered to be due to mainly the effects of the TC asymmetries. The results show that the presence of asymmetries in the 3D run reduces the TC final intensity by about 15% compared with the 2D run, suggesting that the TC asymmetry is a limiting factor to the potential intensity (PI).

In the 2D run without asymmetries, the convective heating in the eyewall generates an annular tower of high potential vorticity (PV) with relatively low PV in the eye. The eyewall tilts outward with height significantly. Underneath the tilted eyewall the downdrafts induced by evaporation of rain and melting of snow and graupel make the subcloud-layer inflow dry and cool, which lowers the boundary layer equivalent potential temperature (θ_e), thus increasing the entropy difference between the air and sea in the vicinity of the radius of maximum wind (RMW). The increased air–sea entropy deficit leads to more energy input into TC from the underlying ocean and thus a greater final intensity. On the other hand, in the 3D run, the model-resolved asymmetric eddies, which are characterized by the vortex Rossby waves in the mid-lower troposphere, play important roles in modifying the symmetric structure of the TC. Potential vorticity and θ_e budgets indicate that significant inward PV mixing from the eyewall into the eye results in a less-tilted eyewall, which in turn limits the drying and cooling effects of downdrafts in the subcloud layer and reduces the air–sea entropy deficit under the eyewall, thereby reducing the TC intensity. The angular momentum budget analysis shows that the asymmetric eddies tend to reduce the strength of the primary circulation in the vicinity of the RMW. This eddy contribution to the azimuthal mean angular momentum budget is larger than the parameterized horizontal diffusion contribution in the 3D run, suggesting an overall diffusive effect of the asymmetric eddies on the symmetric circulation.

1. Introduction

A basic concept in the studies of tropical cyclone (TC) intensity is the potential intensity (PI) that a TC can achieve for a given underlying sea surface temperature (SST) and thermodynamic structure of its environment (Emanuel 1986, 1988, 1995; Holland 1997). Camp

and Montgomery (2001) provided a comprehensive review of available PI theories and suggested that Emanuel's theory comes the closest to providing a useful PI calculation. In Emanuel's PI theory (Emanuel 1986, 1988, 1995), a TC is assumed to be axially symmetric and to behave as a Carnot heat engine, which extracts heat from the warm ocean surface in terms of enthalpy flux and exports it to the environment in the cold upper-tropospheric outflow. The PI is estimated from the air–sea entropy deficit at the ocean surface near the radius of maximum wind (RMW) with the efficiency of the heat engine proportional to the temperature difference between the sea surface and outflow layer. In the latest version, which includes the effect of dissipative heating (Bister and Emanuel 2002a,b), the PI is calculated by the following equation:

* School of Ocean and Earth Science and Technology Publication Number 7045 and International Pacific Research Center Publication Number 435.

Corresponding author address: Dr. Bo Yang, International Pacific Research Center, School of Ocean and Earth Science and Technology, University of Hawaii at Manoa, 1680 East West Road, 401 POST Bldg., Honolulu, HI 96822.
E-mail: yangbo@hawaii.edu

$$V_m^2 = C_p(T_s - T_0) \frac{T_s}{T_0} \frac{C_k}{C_D} (\ln \theta_e^* - \ln \theta_e)|_m, \quad (1)$$

where V_m is the maximum gradient wind at the RMW, C_p is the heat capacity at constant pressure, T_s is the SST under the eyewall, T_0 is the mean outflow temperature, C_k is the exchange coefficient for entropy, C_D is the drag coefficient for momentum, θ_e^* is the saturation equivalent potential temperature at the ocean surface, and θ_e is the boundary layer equivalent potential temperature. The last factor in (1) is evaluated at the RMW with the assumption of constant near surface relative humidity from the environment to the outer edge of the eyewall. Equation (1) can be derived by determining the surface pressure at the RMW with the assumption of gradient wind balance and thermal wind balance at the outer region of the TC. An extensive discussion of the mathematic derivations and the technical issues related to the PI calculation can be found in Bister and Emanuel (2002a). With dissipative heating, the thermodynamic efficiency is $(T_s - T_0)/T_0$ instead of $(T_s - T_0)/T_s$ (the conventional one for a reversible Carnot engine that does work on an external body; Emanuel 1988). Thus, the inclusion of dissipative heating results in a more intense TC. This has been validated by the results from 2D idealized simulation (Bister and Emanuel 1998) as well as 3D real-case simulation (Zhang and Altshuler 1999).

In reality, however, TCs are rarely axisymmetric. The asymmetric structure is generally characterized by quasi-stationary or moving spiral rainbands (Willoughby et al. 1984), vortex Rossby waves (MacDonald 1968; Guinn and Schubert 1993; Montgomery and Kallenbach 1997; Chen and Yau 2001; Wang 2001, 2002a,b), polygonal eyewalls (Lewis and Hawkins 1982; Schubert et al. 1999), and mesovortices embedded in the eyewall (Black and Marks 1991; Willoughby and Black 1996; Kossin et al. 2002; Montgomery et al. 2002). The asymmetric structure in the inner core of a TC can be generated by external forcing, such as the beta effect (e.g., Wang and Holland 1996a,b) and large-scale environmental flow (Shapiro 1983; Li and Wang 1996; Wang and Holland 1996c; Bender 1997; Frank and Ritchie 1999, 2001; Zhu et al. 2004), or internal dynamics (e.g., Schubert et al. 1999).

Although the PI given in (1) does not depend on either the dynamics of the TC eye or the asymmetric structure in the TC eyewall, Emanuel (1989, 1997) showed that certain radial mixing/diffusion of angular momentum is essential for the eye to spin up and for the TC to intensify toward its PI. These radial mixing can be accomplished by asymmetric eddies in the eyewall of real TCs (Montgomery et al. 2002). Neverthe-

less, sensitivity experiments suggested that the evolution of TC is not very sensitive to the magnitude of momentum diffusion in axially symmetric TC models (Emanuel 1989). As long as the TC model is run with a small but nonzero radial diffusion of angular momentum, an initial vortex with finite amplitude can amplify quickly. Only in the ill-posed situation with zero diffusivity, the initial vortex develops slowly and attains intensity well below the theoretical PI. On the contrary, in the case with very large diffusivity, the TC intensity is generally reduced (see Fig. 5 of Emanuel 1989), implying that increase in the level of asymmetries in the eyewall could limit the TC PI. It thus seems that inner-core radial mixing, either parameterized or explicitly resolved by the model, plays a pivotal role in the TC intensification and is a prerequisite for a TC to attain its PI. However, at the later stage, the inner-core asymmetries may limit the intensity of a TC relative to the theoretical PI it would attain in their absence (Montgomery et al. 2002).

The positive role of the asymmetric eddies in TC intensification has been further demonstrated in several recent studies. Heymsfield et al. (2001) documented the asymmetric structure of the intense convection in Hurricane Bonnie (1998) based on multiple observations synthesized from the National Aeronautics and Space Administration (NASA) ER-2 and DC-8 aircraft. They found that significant inner-core asymmetries occurred just before rapid intensification. Montgomery and Kallenbach (1997) proposed that axisymmetrization of asymmetries in the inner-core region could lead a TC vortex to intensify via vortex Rossby wave-mean flow interaction. The possible contribution of asymmetries to the early development and the potential physical mechanisms have been studied by Montgomery and Enagonio (1998) and Möller and Montgomery (1999, 2000). They found that a TC vortex could intensify when convectively generated potential vorticity (PV) anomalies of like sign were ingested into the parent vortex core.

The opposite could be true for mature TCs. Schubert et al. (1999) and Nolan and Montgomery (2002) suggested that direct spindown of the eyewall by eddies resulting from barotropic vortex breakdown could weaken the TC intensity at mature stage. Using a limited-area primitive equation model, Peng et al. (1999) studied the effects of the planetary vorticity gradient (beta) and an imposed uniform mean background flow on TC intensity. They found that the intensity of a TC was inversely proportional to the amplitude of low-level wavenumber-1 asymmetry. The most intense TC evolved on an f plane in a quiescent environment. Inclusion of the beta effect or a uniform background flow

induced a wavenumber-1 asymmetric structure in the inner core and reduced the final intensity. With a hydrostatic primitive equation model, Wu and Braun (2004) investigated the influence of a uniform environmental flow, the beta effect, and vertical shear of the environmental flow on TC final intensity. They showed that the eddy momentum flux associated with inner-core asymmetries could weaken a TC directly by producing a deceleration of the azimuthal mean tangential wind in the vicinity of RMW and indirectly by inducing an anomalous secondary circulation opposite of the primary secondary circulation.

Previous studies have focused mainly on the effect of a specified large-scale environmental flow and suggested that asymmetric structure generated by environmental flow be a dynamical limiting factor to TC intensity at mature stage (Peng et al. 1999; Wu and Cheng 1999; Dengler and Keyser 2000; Frank and Ritchie 2001). However, a clear determination of the mechanism by which the asymmetric structure affects TC intensity remains elusive. The difficulty arises in part from the complexity of TC–environmental flow interaction. Since the asymmetric structure can be generated by internal dynamical processes (Schubert et al. 1999; Chen and Yau 2001; Wang 2001, 2002a,b), questions also arise as to whether, how, and to what degree these internally generated inner-core asymmetries affect TC intensity in the absence of any external forcing. These questions will be addressed in this study through numerical simulations and comprehensive diagnostic analyses.

Several possible processes have been considered that may prevent a TC from achieving its PI predicted by Emanuel's theory. These processes include the adverse effects of vertical wind shear (Gray 1968; Frank and Ritchie 1999, 2001; Zhu et al. 2004), secondary eyewall and full or partial eyewall replacement (Camp and Montgomery 2001; Wang 2002b; Zhu et al. 2004), and upwelling of relatively cold ocean water due to air–sea interaction (Shay et al. 1998; Jacob et al. 2000; see a recent review by Wang and Wu 2004). In contrast, Persing and Montgomery (2003) demonstrated that the axisymmetric model of Rotunno and Emanuel (1987) could produce a storm of increasing intensity while increasing both horizontal and vertical resolution. An upper bound of intensity that greatly exceeds Emanuel's theoretical prediction can be reached when the resolution is sufficiently high. In a 3D real case simulation, Zhang and Wang (2003) have also shown the positive impacts of increasing vertical resolution on hurricane intensity. Persing and Montgomery (2003) further proposed that the entrainment of high entropy air from the eye to the eyewall represents an additional source of

energy input and leads to a modified Carnot cycle that results in a TC with super intensity (see also Holland 1997; Liu et al. 1999). Thus, the PI issue is still an open question that needs further exploration. Since most theories for PI are based upon the axisymmetric assumption, it is essential to identify the impact of removing this constraint on the TC intensity.

We will show in this study that internally generated inner-core asymmetries play a role in reducing the TC PI by modifying the symmetric structure of the storm. This is demonstrated by a comparative study comprising idealized numerical simulations of TCs using a triply nested three-dimensional (3D) TC model and its axisymmetric (2D) version on an f plane in a quiescent environment. The rest of the paper is organized as follows. Section 2 briefly describes the models and the design of the numerical experiments. Section 3 discusses the effects of inner-core asymmetries on both structure and intensity of the simulated TC. In section 4, detailed budget analyses of angular momentum, PV, and θ_e are carried out to reveal physical processes responsible for the simulated TC structure and intensity changes. The major findings are summarized in the last section.

2. The numerical models and experimental design

The 3D numerical model used in this study is the triply nested, movable mesh, tropical cyclone model (TCM3) developed by Wang (1999, 2001, 2002c). It is a hydrostatic primitive equation model in Cartesian coordinates in the horizontal and σ (pressure normalized by surface pressure) coordinate in the vertical. The model consists of 25 σ -layers in the vertical. An integer level is located at the midpoint of each σ -layer and bounded by the half-integer levels. The configuration of the integer σ -levels is shown in Table 1. Horizontal velocity, temperature, geopotential height, and all moist variables are defined at the integer levels, whereas vertical velocity, prognostic turbulence kinetic energy and its dissipation rate, and vertical turbulent fluxes are defined at the half-integer levels. Horizontal resolutions for the three meshes are 45, 15, and 5 km, respectively. A two-way interactive, triply nested, movable-mesh technique is used for time integration. The model physics include an E- ε turbulence closure scheme for subgrid-scale vertical mixing above the surface layer, a modified Monin–Obukhov scheme for the surface-flux calculation and an explicit treatment of mixed-phase cloud microphysics. Subgrid-scale horizontal diffusion is calculated with a fourth-order scheme with the horizontal eddy diffusion coefficient defined by

TABLE 1. Definition of integer σ -levels.

Level index	σ
1	0.01
2	0.03
3	0.05
4	0.07
5	0.09
6	0.115
7	0.15
8	0.195
9	0.25
10	0.31
11	0.37
12	0.43
13	0.49
14	0.55
15	0.61
16	0.67
17	0.73
18	0.79
19	0.845
20	0.89
21	0.925
22	0.951
23	0.971
24	0.9865
25	0.997

$$K_H = \eta_0 d^2 \left(K_{H0} + \frac{1}{2} \eta_1 k^2 d^2 |D| \right), \quad (2)$$

where d is the grid spacing; k is the von Kármán constant (0.4); η_0 is a constant, taken to be 1.0 for all dynamical variables and 0.5 for mixing ratios of all hydrometeors and turbulent kinetic energy and its dissipation rate; η_1 is taken to be 0.6; K_{H0} is a background diffusion coefficient which is a function of grid spacing

$$K_{H0} = \gamma d, \quad (3)$$

where $\gamma = 0.5 \text{ m s}^{-1}$. The deformation of horizontal wind $|D|$ is given by

$$|D| = \left[\left(\frac{\partial u}{\partial x} - \frac{\partial v}{\partial y} \right)^2 + \left(\frac{\partial v}{\partial x} + \frac{\partial u}{\partial y} \right)^2 \right]^{1/2}, \quad (4)$$

where u and v are zonal and meridional winds in Cartesian coordinates, respectively.

A detailed description of TCM3 and its performance and capability of simulating scale interaction in TCs can be found in Wang (1999, 2001, 2002a,b,c). In particular, the model can simulate convectively coupled vortex Rossby waves and their interaction with the primary vortex and related structure and intensity changes (Wang 2002a,b).

To facilitate evaluation of the effect of inner-core asymmetries on TC intensity, an axisymmetric version

of TCM3 is constructed and used in this study as well. The axisymmetric version has the model parameters identical to those in the 3D version. The deformation of the horizontal wind $|D|$ in cylindrical coordinates is given by

$$|D| = \left[\left(\frac{\partial U}{\partial r} - \frac{U}{r} \right)^2 + \left(\frac{\partial V}{\partial r} - \frac{V}{r} \right)^2 \right]^{1/2}, \quad (5)$$

where U and V are radial and tangential winds in cylindrical coordinates, respectively; r is the radial distance. Note that both 2D and 3D models have an identical (and nonzero) momentum diffusion coefficient that fulfills the prerequisite for the model TC to intensify. Thus we will mainly focus on the impact of explicit inner-core asymmetries on the TC intensity at mature stage in this study.

A detailed description of the fourth-order diffusion scheme in cylindrical coordinates is given in appendix A. Mathematically, the horizontal diffusion representations in the two models are equivalent except that one is performed in 2D cylindrical coordinates and the other in 3D Cartesian coordinates. Nevertheless, intrinsic numerical differences in the horizontal diffusion calculations might still exist, prohibiting a firm comparison of the different intensities. In addition, the magnitude of horizontal diffusion depends on the horizontal deformation of the corresponding TCs, a fact that makes the issue even more complex. To target this problem, we designed two additional experiments. One is a 3D experiment in which the deformation is calculated according to Eq. (5) using azimuthally averaged flow. This experiment is used to explore the model sensitivity to 2D or 3D horizontal deformation representation. The other is a 2D experiment, in which the horizontal diffusion is calculated in 3D Cartesian coordinates. Namely, at each time step, we projected the 2D variables, originally cast in cylindrical coordinates, onto Cartesian coordinates, and calculated the horizontal diffusion using Eqs. (2), (3), and (4), and finally projected the calculated tendency due to horizontal diffusion back onto cylindrical coordinates to continue the time integration. By using this approach, we can perform numerically identical horizontal diffusion calculation for the additional symmetric run and the original 3D run, except for the inevitable restriction in the freedom of turbulent processes in the symmetric runs.

Four experiments were thus performed. In the first experiment (hereafter CTL or 3D run), the 3D model was run with 181×161 , 103×103 , 109×109 grid points for the outermost, intermediate, and innermost domains, respectively. In the second experiment (hereafter SYM or 2D run), the axisymmetric model was run

with the horizontal diffusion calculated in cylindrical coordinates. The third experiment (hereafter “an additional 3D experiment”) was the same as the control experiment but with the horizontal deformation calculated by Eq. (5) using azimuthally averaged winds. The fourth experiment (hereafter “an additional symmetric run”) was the same as the second experiment, but with the horizontal diffusion calculated in Cartesian coordinates. The numbers of grid points for the three meshes in the two symmetric runs were 105, 67, and 73, respectively. Note that it is impossible to make the symmetric and 3D versions exactly identical due to geometry, for example, the domain of the 3D model is rectangular while that of the symmetric model is circular. Nevertheless, the domain sizes in the two symmetric runs were intentionally chosen to make the circular areas approximately equal to the corresponding rectangular areas of the 3D model.

In all the four experiments, the model was initialized with an axially symmetric cyclonic vortex that had the surface maximum tangential wind of 20 m s^{-1} at a radius of 100 km. The tangential wind decreased gradually with height and became zero at about 100 hPa. The initial mass and thermodynamic fields were obtained by solving the inverse balance equation in σ -coordinates (Wang 2001). A horizontally uniform SST of 29°C was assumed. The initial water-vapor mixing ratio and environmental sounding were horizontally uniform and representative of the vertical profile of the climatological mean state over the western Pacific (Gray et al. 1975). Since the focus was on the effect of internally generated inner-core asymmetries, an environment at rest with a constant Coriolis parameter f at 18°N was assumed.

3. Effects of inner-core asymmetries on TC intensity and structure

a. TC intensity

Figure 1a shows the evolution of the minimum central pressures in the four experiments. The TC in SYM reaches a minimum central pressure of 890 hPa several times after 120 h, but with significant intensity oscillation. The evolution of minimum central pressure in the additional symmetric run is quite similar to that in SYM, implying that the above-mentioned intrinsic numerical difference in the horizontal diffusion calculation is trivial. In contrast, the TC in CTL reaches a minimum central sea surface pressure of 905 hPa at 139 h and is rather stable afterward, suggesting that the continuous mixing due to the asymmetric eddies in the eyewall may reduce the high-frequency intensity oscillation. At mature stage, the evolution of the minimum

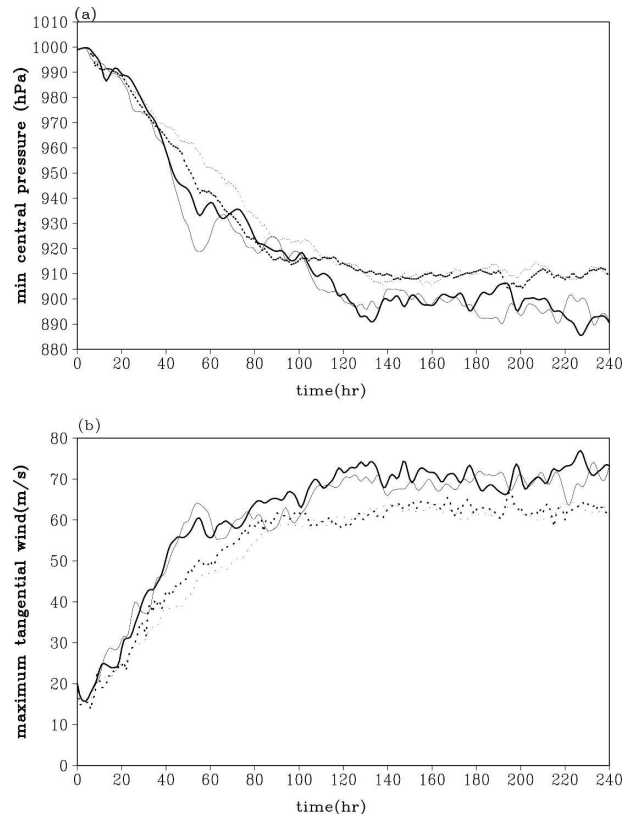


FIG. 1. Time evolution of (a) the minimum central surface pressure (hPa) and (b) the maximum azimuthal mean tangential wind (m s^{-1}) at the lowest model level for the simulated storms in CTL (dotted line), SYM (thin solid line), the additional symmetric run (dark solid line), and the additional 3D run (dark dotted line).

pressure in the additional 3D run is quite similar to that in CTL, indicating that the TC intensity is not sensitive to the asymmetries in deformation fields in the simulation. Consistent with the minimum central surface pressure difference, the maximum azimuthal mean tangential winds in the two symmetric experiments are also larger than those in the two 3D experiments during the mature stage.

The asymmetric vorticity dynamics in the TC's eye and eyewall region has been related to the barotropic instability near the RMW (Schubert et al. 1999; Wang 2001). However, this kind of instability cannot be released in two symmetric runs due to the symmetric assumption. Instead, the vortex in two symmetric runs exhibit a high-frequency oscillation with radial displacement of convective rings in the TC core region due to the high inertial stability $\{I = \sqrt{[(\partial V/\partial r) + (V/r) + f][(2V/r) + f]} \gg f\}$ (Shapiro and Montgomery 1993).

A standard FORTRAN subroutine provided by Emanuel (Bister and Emanuel 2002a; downloaded from <http://wind.mit.edu/~emanuel/home.html>) was

used to calculate the theoretical PI. The SST and the environmental sea level pressure used for calculation are 29°C and 1010 hPa, respectively, as in the numerical simulations. Correspondingly, the Gray sounding (Gray et al. 1975) is utilized in the PI calculation. The inflow boundary layer relative humidity is assumed to be the same as that of the environment (RH = 86%). As seen from Eq. (1), the maximum azimuthal wind (and thus the central pressure deficit) of TCs depends on the ratio of entropy to momentum exchange coefficients (C_k/C_D). Emanuel (1995) suggested that in real TCs this ratio lies in the range 0.75–1.5. In TCM3, C_k/C_D varies with wind speed and is about 0.55 near the RMW, which is used in our PI calculation. Note also that dissipative heating is included in the PI calculations as in our numerical model, and a default factor of 0.8 in Emanuel's standard FORTRAN program is applied in the calculation of maximum tangential wind to account for the wind speed reduction in the boundary layer from the gradient level. This factor applies reasonably well in our 2D and 3D simulations. Specifically, in the 2D model, the maximum tangential wind at the surface is around 70 m s⁻¹ (Fig. 1b) and the maximum wind at the top of boundary layer is about 88 m s⁻¹ (Fig. 3a), respectively; whereas in the 3D model, the maximum at the surface is around 62 m s⁻¹ and that at the top of boundary layer is about 78 m s⁻¹ (Fig. 3b).

Given these specified parameters, the PIs in terms of the central pressure and maximum wind speed are 917 hPa and 58 m s⁻¹, respectively. Therefore, the intensities in both 2D and 3D runs exceed Emanuel's theoretical PI. This PI excess has been termed superintensity by Persing and Montgomery (2003). Nevertheless, there is always uncertainty in this type of PI calculation. For example, in the PI calculation, T_0 is taken as the temperature at an equilibrium level for a surface air parcel lifted in Gray's environmental sounding, which strictly speaking is not the outflow temperature of Emanuel's PI theory, but just a reasonable approximation. The difficulty and ambiguity in determining parameters in the PI calculation have been extensively discussed by Persing and Montgomery (2003). In this regard, it is not our attempt to compare the numerical results with theory quantitatively. Rather, we discuss Emanuel's PI theory only to reveal the physical mechanisms behind the model results.

The TC intensities at the mature stage in the two 3D runs are about 15% weaker in terms of the maximum surface wind than those in the two symmetric experiments. This suggests that internally generated inner-core asymmetries play a similar role as the externally forced inner-core asymmetries and limit the TC maximum intensity. In addition to having a higher maximum

intensity, the storms in the two symmetric simulations intensify more rapidly than those in the two 3D simulations. Although our analysis below mainly focuses on mature stage, the mechanisms we proposed can also explain the difference in intensification rates as presented in Fig. 1. Note also that the difference between SYM (CTL) and the additional symmetric experiment (the additional 3D experiment) is quite small and does not change the central conclusion drawn in this study. To avoid redundancy, we focus only on the comparison between SYM and CTL in the following analyses.

b. Inner-core asymmetric structure

Even for the simulation starts from an axisymmetric incipient vortex in an environment at rest on an f plane, small amplitude of asymmetries can be generated from finite differencing and lateral boundary conditions. In dry cases, those numerical errors are negligibly small and do not exert any meaningful impact on the intensity change of the TC (figure not shown). However, in the 3D full physics model run performed in this study, diabatic heating redistributes PV, resulting in a reversal of the sign of the radial PV gradient of the symmetric vortex, thereby satisfying the necessary condition for linear instability to asymmetric disturbances (Schubert et al. 1999). Nolan and Montgomery (2002) investigated the linear dynamics of perturbations to TC-like vortices. They found that intense TC-like vortices were unstable to low wavenumber perturbations, whereas the weaker TC-like vortices were stable to all azimuthal wavenumbers. In addition, Smith and Montgomery (1995) identified an inviscid wavenumber-selection mechanism that favored the decay of high wavenumber perturbations over low wavenumber perturbations in TC-like vortices. The studies by Chen and Yau (2001) and Wang (2002a,b), who used full physics models, also confirmed the presence of low-azimuthal-wavenumber disturbances characterized by vortex Rossby waves. Although the origin of asymmetries might arise from finite differencing and lateral boundary conditions, its structure and evolution is controlled by the internal dynamic instabilities in the inner-core region. In this regard, without any confusion, we refer to the model asymmetries in the 3D runs as internally generated inner-core asymmetries.

As examples, Figs. 2a,b show the total asymmetric geopotential height and horizontal wind fields at 850 hPa, after 209 and 173 h of simulation in CTL, respectively. The asymmetries in both geopotential height and horizontal winds are dominated by low wavenumber structure in the inner-core region (wavenumber 1 in Fig. 2a and wavenumber 2 in Fig. 2b), with the maximum amplitude near the RMW. The divergent anticy-

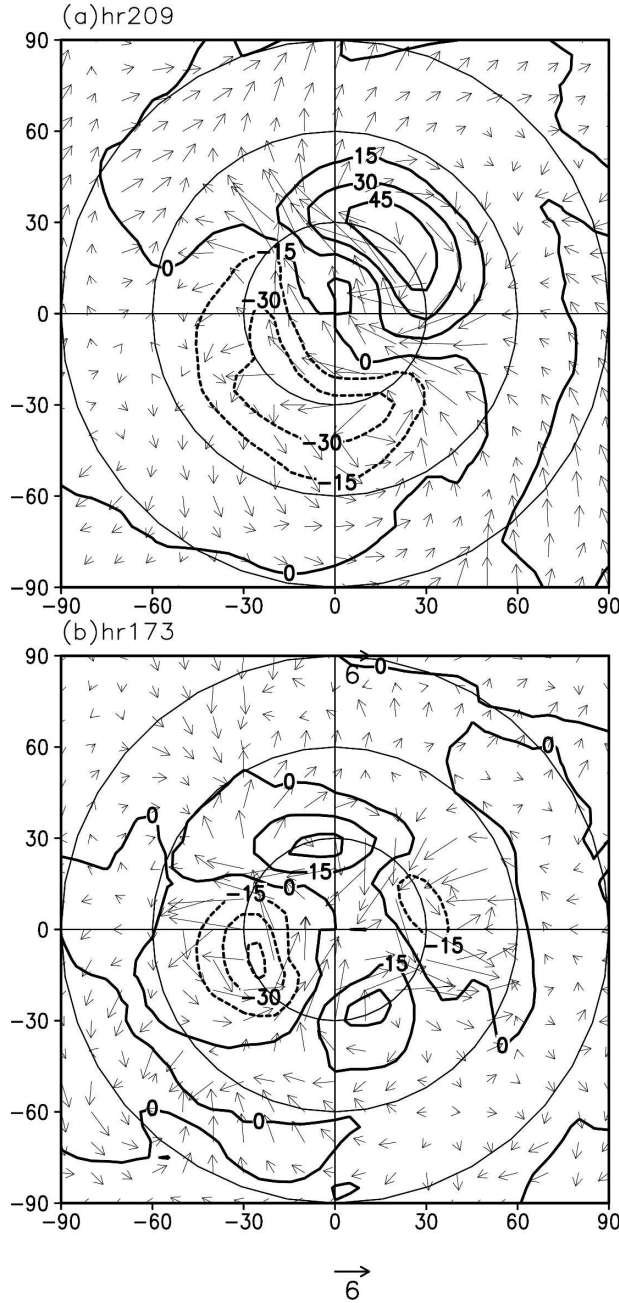


FIG. 2. Total asymmetric geopotential height (contours, $\text{m}^2 \text{s}^{-2}$) and horizontal wind (arrows, m s^{-1}) fields at 850 hPa after (a) 209 h and (b) 173 h of simulation, respectively. The domain shown in each panel is $180 \text{ km} \times 180 \text{ km}$. Circles depict radii at every 30 km from the TC center.

clonic flow is collocated with the positive perturbation geopotential height, and the confluent cyclonic flow is collocated with the negative perturbation geopotential height. Wang (2001, 2002a,b) identified these asymmetries as convectively coupled vortex Rossby waves. Since the difference between the 3D and 2D runs is the

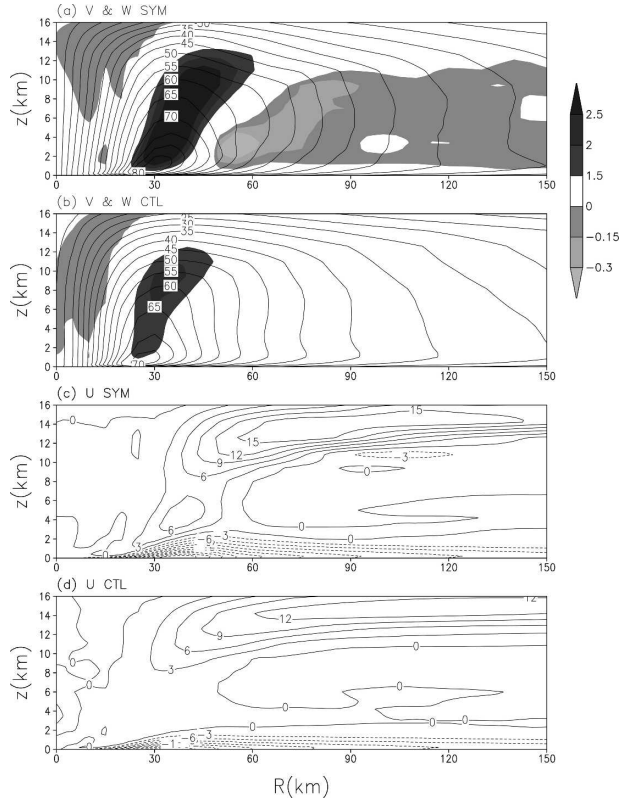


FIG. 3. Composite (120–240 h averaged) axisymmetric structure of the simulated storm at the mature stage in experiments SYM and CTL. Shown are radial–height cross sections of the azimuthal mean tangential winds, V (contoured) and vertical motion, W (shaded) for (a) SYM and (b) CTL; radial winds, U (contoured) for (c) SYM and (d) CTL. Contour intervals are 5 m s^{-1} for tangential wind and 3 m s^{-1} for radial wind. Values greater than 1.5 m s^{-1} (negative values) are heavily (lightly) shaded for vertical motion fields. Note that shading intervals are -0.3 , -0.15 , 0 , 1.5 , 2 , and 2.5 m s^{-1} , respectively.

presence of asymmetric motion in 3D, and its absence in 2D, it should be the asymmetric motion that interacts with and modifies the symmetric component of the TC, affecting the TC intensity.

c. Time-mean symmetric structure

To understand how the asymmetric structure affects TC intensity, the symmetric structures of the simulated TCs in the SYM and CTL runs were first compared. Figure 3 shows the time mean symmetric structure of the simulated TCs based on the hourly output averaged between 120 and 240 h. The overall symmetric structure in CTL is similar to that in Fig. 3 in Liu et al. (1999). The tangential wind in CTL is weaker in the eyewall but stronger inside the eyewall than in SYM (Figs. 3a,b). Consistent with its weaker intensity (Fig. 1), the radial inflow in the boundary layer and outflow in the

upper troposphere are also weaker in CTL (Figs. 3c,d). Although strong upward motion occurs in the outward tilted eyewall (Figs. 3a,b) in both simulations, it is much stronger in the more intense TC in SYM. Furthermore, the eyewall slope in SYM is greater below 6 km with considerable mesoscale downdrafts under the tilted eyewall.

Figures 4a,b show the symmetric condensational heating rates in SYM and CTL, respectively. The maximum heating rate in the eyewall in SYM is almost as twice large as that in CTL and shows a more outward-tilted vertical distribution. The negative value under the tilted eyewall indicates cooling due to evaporation of rainwater and melting of snow and graupel. Clearly, the cooling rate is more pronounced in SYM due to a greater outward eyewall tilt in the mid-lower troposphere than in CTL (Figs. 4a,b). The effects of downdrafts are evident from examination of the relative humidity field, which is relatively lower in the boundary layer just outside the eyewall in SYM (Fig. 4c) than in CTL (Fig. 4d). The equivalent potential temperature [defined as $\theta_e = \theta \exp(Lq_v/C_p T)$, where θ is the potential temperature, L the latent heat of condensation, q_v the water vapor mixing ratio, C_p the specific heat at constant pressure, and T the temperature; see Rotunno and Emanuel (1987), p. 544] under the tilted eyewall is also lower in SYM (Figs. 4e,f) as a result of both drying and cooling effects of downdrafts. The differences in the eyewall tilt and the associated mesoscale downdrafts are robust in instantaneous snapshots (figure not shown) and thus are a distinct feature that is responsible for the difference in TC intensity between the 3D and 2D runs.

Throughout the troposphere, the radial–height distribution of the azimuthal mean PV in SYM shows an annular tower of high PV with relatively low PV within the eye (Fig. 4g). In contrast, the azimuthal mean PV in CTL shows a monotonic distribution in the mid-upper troposphere while displaying an off-centered maximum in the lower troposphere (Fig. 4h). The difference in the azimuthal mean PV distribution in CTL and SYM is mainly due to the presence of the resolved eddy mixing process in CTL. As seen from Fig. 2, the TC in the 3D run develops considerable asymmetric eddies that are characterized by convectively coupled vortex Rossby waves in the inner-core region; the corresponding development in SYM is prohibited due to the reduced geometry. These asymmetric eddies in the 3D run play an important role in mixing PV and angular momentum between the eyewall and the eye (Wang 2002a,b). Because of low inertial stability and the lack of local PV sources, such PV mixing is most significant in the

mid-upper troposphere, where it results in a nearly monotonic PV distribution. However, continuous PV generation associated with condensational heating (Fig. 4b) tends to offset PV mixing partially and sustains an off-centered PV maximum in the mid-lower troposphere. In contrast, the horizontal PV rearrangement process is lacking in SYM, thus sustaining an off-centered PV maximum throughout the troposphere (Fig. 4g).

The question arises as to what causes the smaller outward tilt of the eyewall. The eyewall ascent in a TC primarily follows the absolute angular momentum (AAM) surface (Emanuel 1988, 1995). The asymmetric eddies play a role in mixing not only PV but also AAM between the eyewall and the eye (Wang 2002b). This eddy mixing diminishes the AAM gradient near the RMW and increases the gradient on either side of it. Hence, the AAM gradient in the mid-upper troposphere inside the eyewall will increase as a result of the eddy mixing. Since the AAM at the TC center is zero by definition, an increased AAM gradient in the mid-upper troposphere will naturally pull the isolines of AAM toward the eye side, resulting in a less tilted eyewall than in SYM. This is also evident in the azimuthal mean tangential wind shown in Figs. 3a,b. Note that the PV surface in Figs. 4g,h outside the eye also follows the tilted eyewall, indicating that the PV surface can also be used as a proxy of the eyewall ascent angle. Therefore, the lateral eddy mixing of both PV and AAM in the mid-upper troposphere considerably modifies the eyewall ascent angle in the 3D run (see also budget analyses in section 4).

d. Eyewall tilt and TC maximum intensity

A key factor that determines the maximum TC intensity is the entropy deficit at the ocean surface near the RMW (Emanuel 1989, 1995). In SYM, the downdrafts under the tilted eyewall dry and cool the subcloud layer (Figs. 4c,e), lowering the boundary layer entropy and increasing the air–sea entropy deficit at the RMW and thus TC maximum intensity. In CTL, PV rearrangement in the mid-upper troposphere results in a less tilted eyewall (Fig. 3b); the downdrafts are weaker as a result of higher subcloud-layer relative humidity under the eyewall and a lower cloud base (Figs. 4b,f). The air–sea entropy deficit near the RMW and thus the final TC intensity in CTL are reduced. The θ_e near the RMW in the boundary layer in SYM is around 357 K, which is slightly lower than that in CTL (359 K; Figs. 4e,f). When the lower pressure and thus higher θ_e^* at the sea surface in SYM are taken into account, the local entropy deficit near the RMW is definitely higher, consistent with the mechanism proposed above.

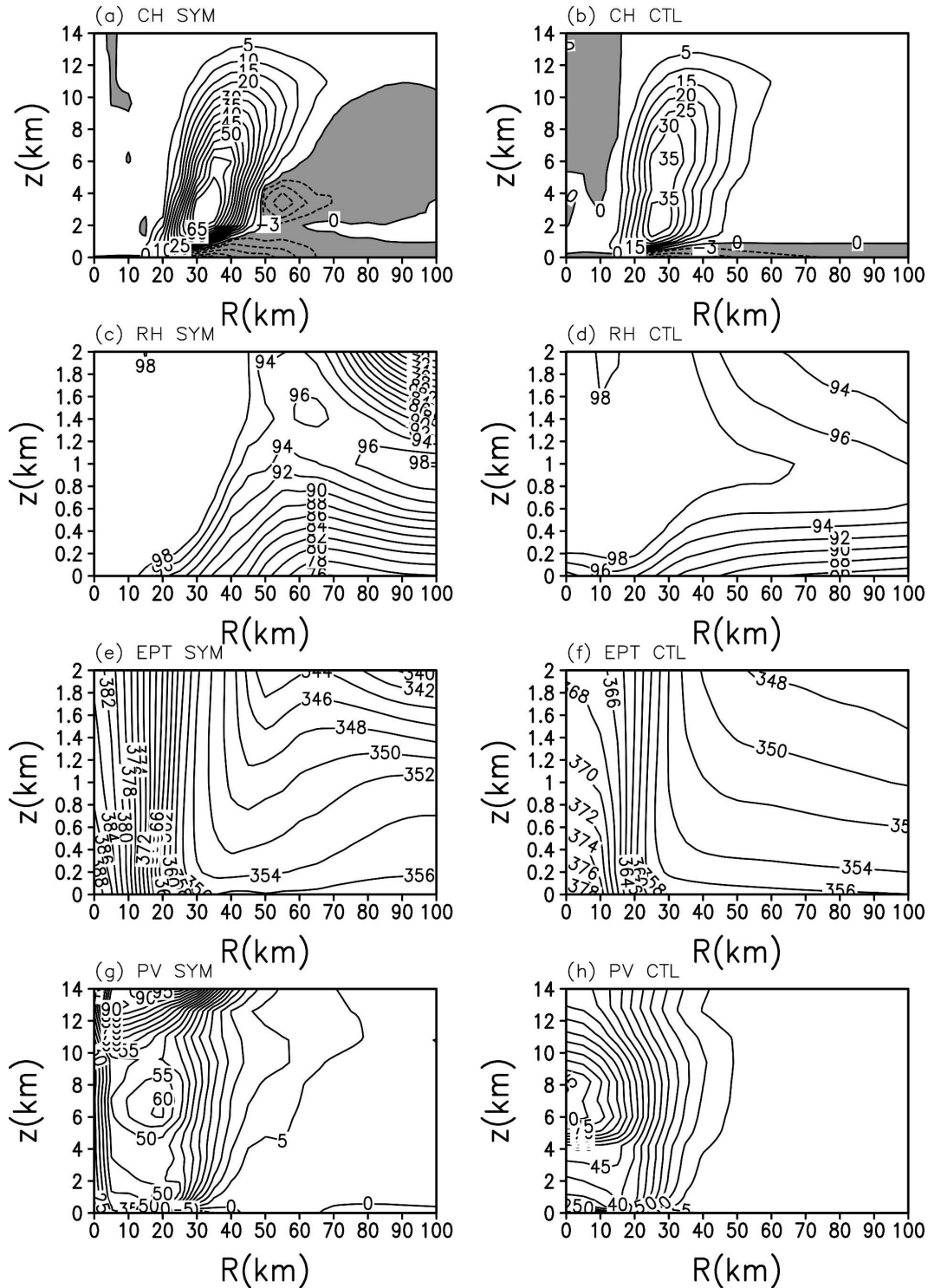


FIG. 4. As in Fig. 3 but for total condensational heating rate, CH (K h^{-1}), relative humidity, RH (%), equivalent potential temperature, EPT (K), and PV [potential vorticity units (PVU, where $1 \text{ PVU} = 10^{-6} \text{ m}^2 \text{ s}^{-1} \text{ K kg}^{-1}$)] for (a), (c), (e), (g) SYM and (b), (d), (f), (h) CTL. Note that the vertical axis is (a), (b), (g), (h) 0–14 and (c), (d), (e), (f) 0–2 km in height.

In Emanuel's PI theory, the relative humidity of the inflow layer is assumed to be the same as that of the environment. Obviously, this does not strictly hold, as seen in Figs. 4c,d. Nevertheless, the area-averaged relative humidity at the lowest model level in the eyewall is approximately 86% in SYM but about 90% in CTL. Using Emanuel's approach, the PI in terms of the central pressure and maximum wind speed are 929 hPa and 54 m s^{-1} , for the elevated relative humidity in CTL. The difference in the final intensity in the 2D and 3D runs is largely determined by the difference in the entropy deficit at the air-sea interface in the vicinity of the RMW.

Consistent with the intensity and structure difference in the two simulations, the total surface heat flux (sensible heat and latent heat fluxes) between 25 and 70 km radii is larger in SYM than in CTL (Fig. 5a). Although considerable evaporation under the tilted eyewall reduces the precipitation efficiency somewhat, the precipitation rate under the eyewall is still larger in the SYM run than in the CTL run; the opposite is true outside the eyewall (Fig. 5b).

Figures 6a,b shows the Hovmöller diagrams of the azimuthal mean vertical velocities at 2 km height in SYM and CTL, respectively. The downdrafts just outside the eyewall are much stronger in SYM than in CTL. Taking into account the decreased precipitation rate in the same region, we can consider the enhanced downdrafts being associated with low-precipitation-efficiency clouds. Emanuel (1989) discussed the different roles of clouds with low-precipitation efficiency and high-precipitation efficiency. The former stabilize the atmosphere mainly through importing low θ_e air into the subcloud layer, while the latter stabilize the atmosphere mainly by heating the free troposphere. In the SYM run, low-precipitation-efficiency clouds just outside the eyewall play an important role in keeping the boundary layer relative humidity and θ_e relatively low, maximizing the entropy deficit at the air-sea interface near the RMW and thus the TC intensity.

Previous studies argued that downdrafts from outer spiral rainbands could limit TC intensity (e.g., Barnes et al. 1983; Powell 1990a,b). First, downdrafts bring dry and cool air with low θ_e from the midtroposphere into the inflow boundary layer. The air with low θ_e is advected to the core region by the boundary layer inflow and entrained into the eyewall, thus suppressing eyewall convection and reducing the TC intensity. Second, downdrafts have a barrier effect on the boundary layer inflow, reducing both mass and moisture convergence into the eyewall, and thus suppressing the eyewall updrafts and eyewall convection, and reducing TC intensity. As a result, active spiral rainbands and associated

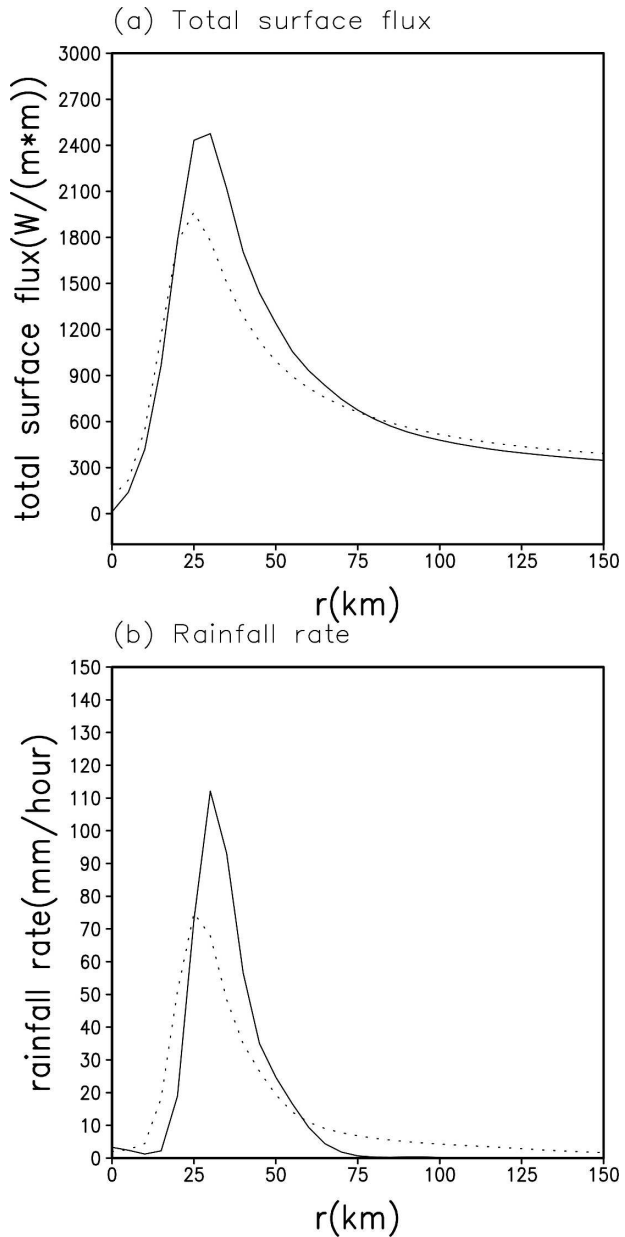


FIG. 5. Composite (120–240 h averaged) radial profiles of (a) total surface heat flux (sensible plus latent heat fluxes, W m^{-2}) and (b) rainfall rate (mm h^{-1}). Solid line is for SYM and dotted line is for CTL.

strong downdrafts can be regarded as an inhibiting factor to TC intensity (Wang 2002c). The downdrafts from a tilted eyewall in this study, however, have a different effect from those in outer spiral rainbands: they neither destroy the eyewall convection nor act as a barrier to the boundary layer inflow, but maintain the air-sea entropy deficit in the vicinity of the RMW and thus strengthen the TC.

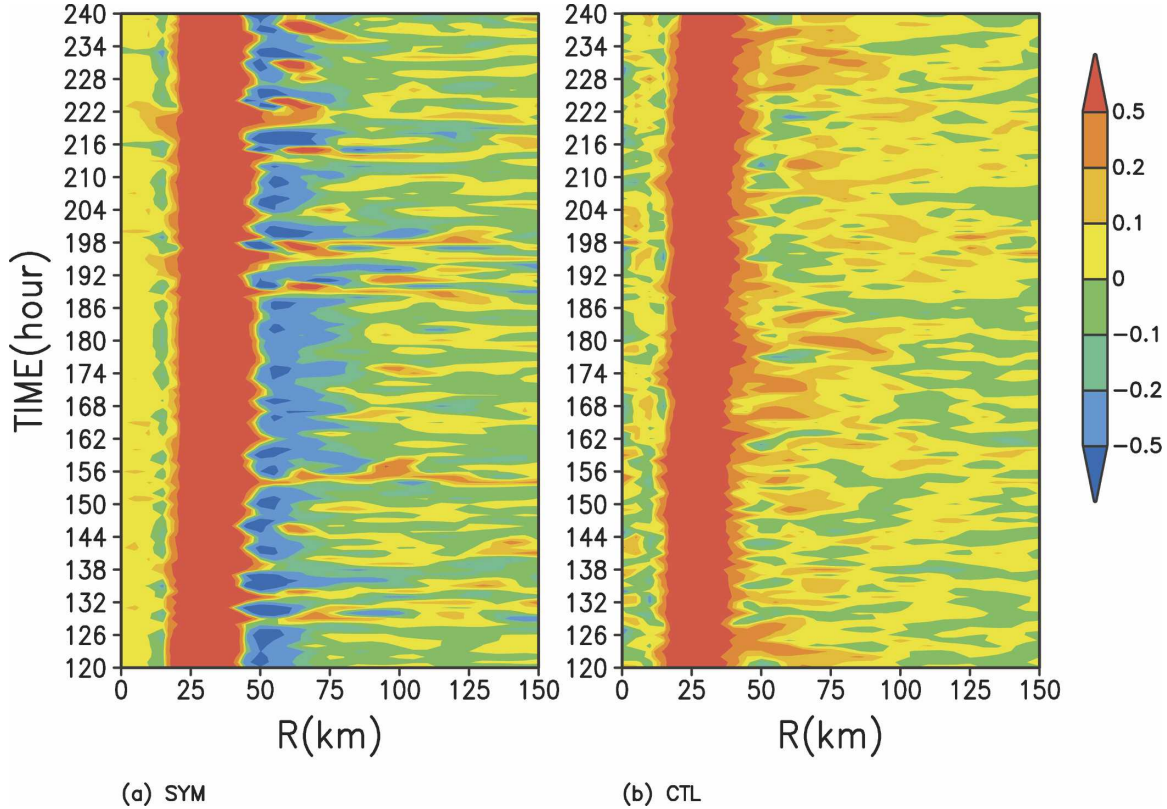


FIG. 6. Hovmöller diagram of azimuthal mean vertical velocity (m s^{-1}) at the height of 2 km for (a) SYM and (b) CTL, respectively.

4. Budget analyses

To further understand the interaction between the asymmetric and symmetric components and its effect on the simulated TC intensity, we have performed budget analyses for the azimuthal mean relative angular momentum (RAM), PV, and θ_e . Detailed descriptions of these budget equations are given in appendix B. All the budgets given below are based on the hourly outputs averaged between 120 and 240 h. The results, however, are not sensitive to the temporal resolution of the output.

a. Angular momentum budget

The local change in azimuthal mean RAM is determined by four processes [see appendix, (B1)]: advection of the azimuthal mean AAM (Coriolis torque included) by symmetric (mean) flow; vertical turbulent mixing, including the surface friction; horizontal diffusion; and the horizontal and vertical eddy contribution, which plays a role equivalent to the horizontal diffusion. Figures 7 and 8 show the time mean radial–height cross sections of different terms in the azimuthal mean RAM budget for the SYM and CTL runs, respectively.

In both simulations, the contribution by symmetric advection is mainly balanced by surface friction and vertical mixing in the boundary layer in the inner-core region. The contributions by symmetric advection and frictional torque are both smaller in CTL than in SYM mainly because of the reduced primary and secondary circulations in CTL (Figs. 7a,b and 8a,b).

In both SYM and CTL experiments, the parameterized horizontal diffusion spins up the tangential flow on both sides of the RMW at the expense of weakening tangential winds near the RMW. In the lower troposphere, the positive azimuthal mean RAM tendency on both sides of the eyewall is much larger in SYM than in CTL (Figs. 7c and 8c,d). At the finest resolution of 5 km used in our experiments, the parameterized horizontal diffusion contribution in CTL becomes weaker in the azimuthal mean RAM budget than the explicit eddy contribution (Figs. 8c,d). In particular, resolved eddies spin down the tangential winds over a wide area under the eyewall in the boundary layer while spin up the tangential winds inside the RMW (Fig. 8d), consistent with the results of Wang (2002b) and Wu and Braun (2004). In the azimuthal mean RAM budget, the sum of the parameterized horizontal diffusion and explicit

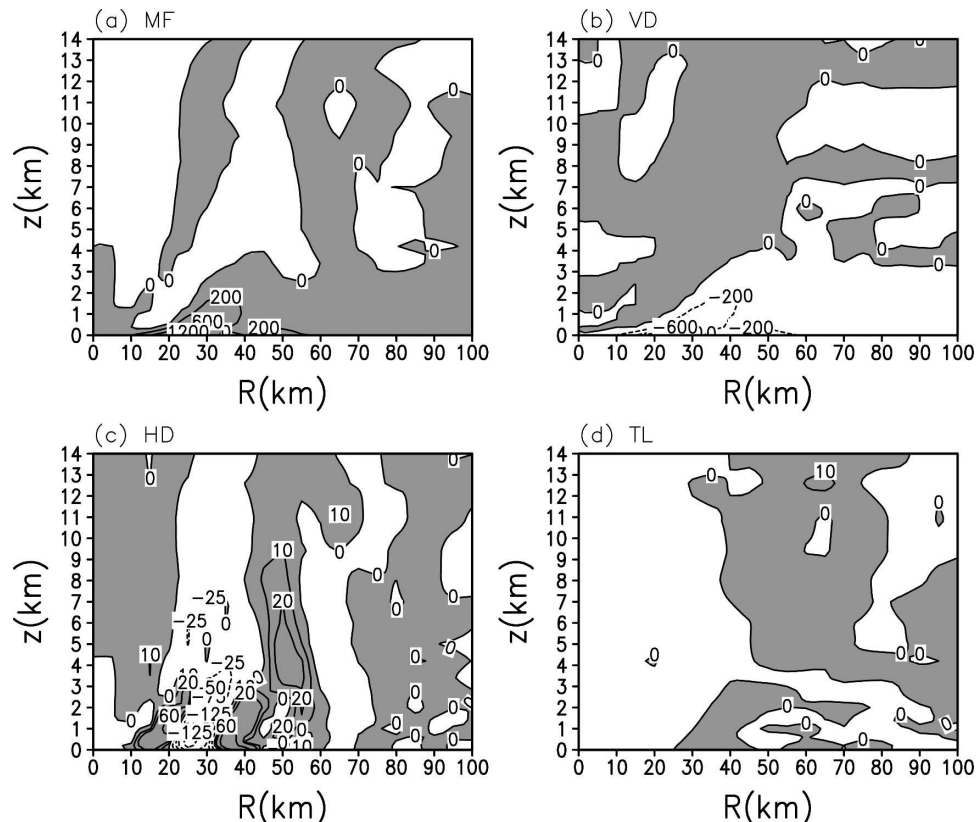


FIG. 7. Composite (120–240-h averaged) radial–height cross sections of azimuthal mean angular momentum budget for SYM. Four panels correspond to contributions to the local rate-of-change of mean angular momentum by (a) symmetric (mean) flow advection, MF; (b) subgrid-scale vertical diffusion, VD; (c) horizontal diffusion, HD; and (d) total, TL, respectively. Units are $\text{m}^2 \text{s}^{-2}$. Contours are 0, ± 200 , ± 600 , $\pm 1200 \text{ m}^2 \text{s}^{-2}$ in (a) and (b), -125 , -50 , -25 , 0 , 10 , 20 , $60 \text{ m}^2 \text{s}^{-2}$ in (c), and $10 \text{ m}^2 \text{s}^{-2}$ in (d). Shading represents regions with positive values. Note that the residual (TL) is much smaller than individual term.

eddy mixing in CTL contributes to a negative tendency under the eyewall in the boundary layer with a magnitude similar to the parameterized horizontal diffusion alone in SYM. Note that the similar spinning-down rate of azimuthal mean RAM for the weaker storm in CTL implies a relatively larger negative effect by parameterized horizontal diffusion and explicit eddy mixing in CTL.

A significant feature of the resolved eddies in the CTL run is its contribution to a positive azimuthal mean RAM tendency just inside the eyewall (between 10 and 25 km radii) within a vertical layer between heights of 1 and 8 km (Fig. 8d). Although small in magnitude, this positive RAM tendency is dynamically important and plays a critical role in reducing the outward tilt of the AAM surface in CTL compared to that in SYM. Since the eyewall ascent mainly follows the AAM surface in the free troposphere (Emanuel 1988, 1995), this explains the less outward eyewall tilt in CTL

than that in SYM, as previously discussed in section 3c. However, it should also be noted that in the lowest 3 km, the eyewall ascent does not follow the AAM well because of the pronounced mixing in the boundary layer.

b. PV budget

In section 3, we also attributed the less-outward vertical tilt of the eyewall in CTL to the PV mixing by asymmetric eddies. This process can be measured by the contribution of asymmetric eddies to the azimuthal mean PV budget. Figures 9 and 10 show the composite radial–height cross sections of different terms in the azimuthal mean PV budget for SYM and CTL, respectively. The definitions of individual terms can be found in appendix B.

In both SYM and CTL, positive (negative) PV tendency is generated below (above) the level of maximum heating (at around 3.5 km) and is mainly balanced by

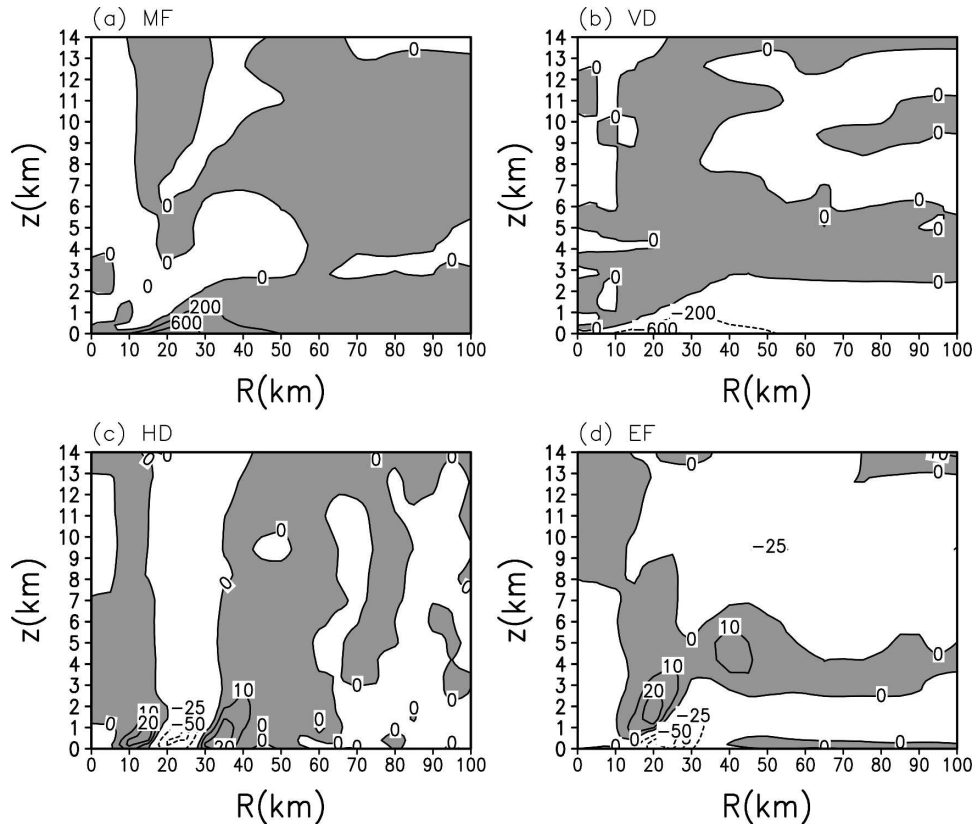


FIG. 8. As in Fig. 7 except for CTL and (d) asymmetric eddies, EF. Contours are -125 , -75 , -50 , -25 , 0 , 10 , 20 , $60 \text{ m}^2 \text{ s}^{-2}$ in (c) and (d).

the transport of azimuthal mean PV due to the azimuthal mean circulation. Consistent with previous studies by Wu and Kurihara (1996) and Wu (2001), the strong updrafts in the eyewall lead to condensation of moist air, which acts as a local PV source/sink on one hand, and transport of PV upward, redistributing PV on the other hand. Note that the parameterized vertical and horizontal diffusion has little effect on the PV budget except for in the near surface layer in both runs.

A distinct feature is found in CTL run, where the resolved asymmetric eddies transport PV from the eyewall both inward and outward in the low levels in the core region (Fig. 10d). In the mid-upper troposphere between 5 and 8 km heights, eddies contribute to a positive PV tendency in the eye region, indicating an inward PV mixing. Although quite small in magnitude, the contribution by the eddy processes is dynamically important as the eddies transport PV inward between 5 and 8 km heights, reducing the outward eyewall tilt, as indicated in section 3d. The small contribution from eddy mixing also reflects a monotonic PV distribution in the mid-upper troposphere at the mature stage of the TC in CTL (Fig. 4h).

c. θ_e budget

The θ_e budget is derived following Rotunno and Emanuel (1987) [see appendix B, (B7)–(B17)]. Figures 11 and 12 show the composite radial–height cross sections of different terms in the azimuthal mean θ_e budget for the SYM and CTL runs, respectively. In SYM, consistent with the theory of Emanuel, the contribution by mean horizontal advection is mainly balanced by vertical mixing including the enthalpy flux at the ocean surface between the inner edge of the eyewall and the RMW in the boundary layer. In particular, the θ_e budget under the eyewall in the boundary layer is dominated by the surface enthalpy flux and radial cold advection of θ_e . The contribution by vertical advection is small and tends to offset horizontal advection (Fig. 11). Another distinctive feature for vertical advection is a negative tendency outside the RMW near the top of the boundary layer. As discussed in section 3, this negative tendency is associated with the downdrafts underneath the tilted eyewall and it plays an important role in importing low θ_e air into the subcloud layer, maintaining a large entropy deficit at the air–sea interface near the RMW.

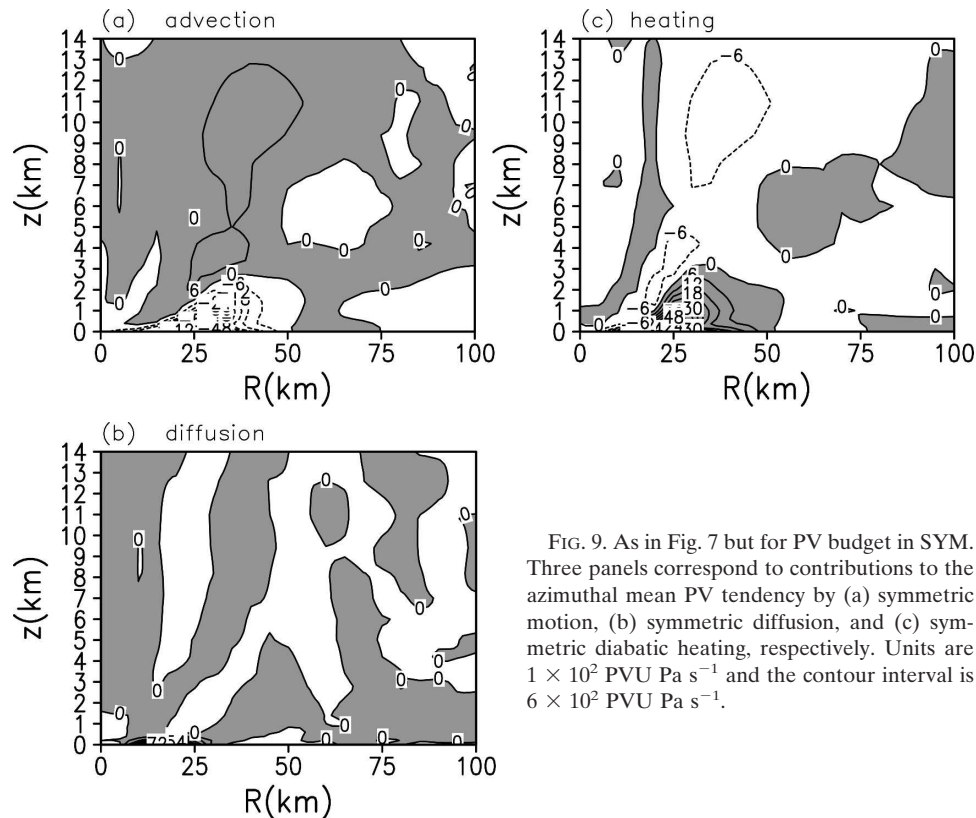


FIG. 9. As in Fig. 7 but for PV budget in SYM. Three panels correspond to contributions to the azimuthal mean PV tendency by (a) symmetric motion, (b) symmetric diffusion, and (c) symmetric diabatic heating, respectively. Units are 1×10^2 PVU Pa s^{-1} and the contour interval is 6×10^2 PVU Pa s^{-1} .

In CTL, a similar balance occurs between the surface enthalpy flux and mean radial cold advection of θ_e under the eyewall (Fig. 12). However, vertical advection doesn't show considerable negative tendency outside the RMW near the boundary layer top, as seen in SYM. Without significant downward θ_e advection into the boundary layer, relative humidity increases gradually as the air parcel spirals inward, resulting in higher boundary layer θ_e and a smaller entropy deficit at the air–sea interface near the RMW, implying a weaker final storm intensity in CTL than in SYM. Note that contributions by the horizontal eddy processes are primarily negative in the lower troposphere in the inner-core region, and thus unfavorable to TC intensity.

Another important feature in the θ_e budget is the contribution of the parameterized horizontal and vertical diffusion, which shows an upward and outward mixing (entrainment) of high θ_e air from the surface layer inside the eyewall (Figs. 11c and 12c). Persing and Montgomery (2003) demonstrated that this entrained high θ_e from the eye to the eyewall represents an additional source of energy input and leads to a modified Carnot cycle and thus a superintense storm. As we discussed in section 3a, both storms in CTL and SYM are superintense. Our results therefore are consistent with Persing and Montgomery's findings. Note that the pa-

rameterized mixing here contributes positively to the TC intensity. In particular, this mixing is larger in SYM run than that in CTL run, consistent with the stronger storm in the former. It should be pointed out that the larger mixing in SYM than in CTL is a result of the storm structure and energy input from the ocean, both are affected considerably by the 3D asymmetric eddies in CTL as discussed in section 3. The 3D eddies themselves also directly contribute negatively to the θ_e budget in the eyewall (Fig. 12d).

5. Summary and discussion

a. Summary of the results

The effect of internally generated inner-core asymmetries on TC intensity is investigated by comparing simulations from a 3D TC model and its axisymmetric version. Both 3D and axisymmetric runs have nearly identical model structures and parameters and are integrated from the same initial conditions on an f plane in an environment at rest. It is shown that the internally generated inner-core asymmetries limit the maximum TC intensity, reducing the maximum intensity by as much as 15% in the case studied. Angular momentum, PV, and θ_e budgets for the simulated storms are con-

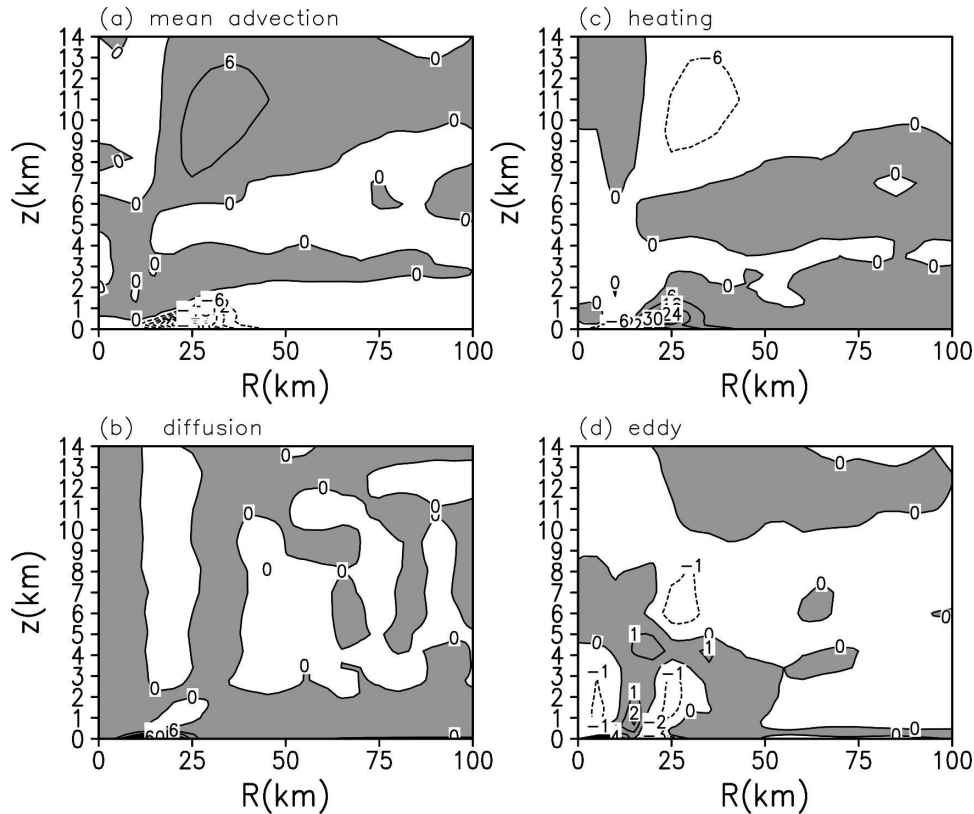


FIG. 10. As in Fig. 9 but for CTL. Four panels correspond to contributions to the azimuthal mean PV tendency by (a) symmetric (mean) motion, (b) symmetric (mean) diffusion, (c) symmetric (mean) diabatic heating, and (d) asymmetric eddy. Contour intervals are 6×10^2 PVU Pa s^{-1} in (a), (b), (c) and 1×10^2 PVU Pa s^{-1} in (d).

ducted to understand how the inner-core asymmetries limit TC intensity.

The physical mechanisms responsible for the difference in the simulated TC intensity are identified through comprehensive diagnostic and budget analyses and are schematically summarized in Fig. 13. Diabatic heating in the eyewall tends to produce an annular tower of cyclonic PV with a maximum just inside the eyewall, where the radial PV gradient changes sign and satisfies the necessary condition for barotropic instability. The release of barotropic instability generates asymmetric eddies, facilitating inward angular momentum transport and PV mixing in the mid-upper troposphere. These processes reduce the slope of the outward eyewall tilt, which in turn reduces the formation of mesoscale downdrafts below the eyewall, and the cooling and drying of the subcloud layer. As a result, the air-sea entropy deficit under the eyewall decreases, so does the energy input to the TC heat engine (Emanuel 1988), limiting the TC final intensity.

The angular momentum budget shows that at the resolution of 5 km used in this study, the explicit eddy

mixing dominates the parameterized horizontal diffusion in the 3D model. The sum of these two terms of the azimuthal mean angular momentum in CTL contributes to a negative tendency in the eyewall region with a magnitude similar to the parameterized horizontal diffusion alone in SYM. The fact that they have a similar magnitude implies a greater negative impact for the weaker storm in CTL. Therefore, consistent with previous theoretical studies of Schubert et al. (1999), Nolan and Montgomery (2002), and budget analyses by Wang (2002b) and Wu and Braun (2004), eddies in the 3D experiment tend to reduce the winds near the RMW and thus reduce the TC intensity. More importantly, the inward eddy transport of angular momentum in the inner-core region in the mid-upper troposphere also reduces the outward slope of the angular momentum surface, resulting in a reduced eyewall ascent angle and thus a smaller outward tilt of the eyewall than in SYM.

The PV budget analysis verifies the hypothesis that the horizontal eddies in the inner-core region play an essential role in PV mixing between the eyewall and the eye, maintaining a monotonic PV distribution in the

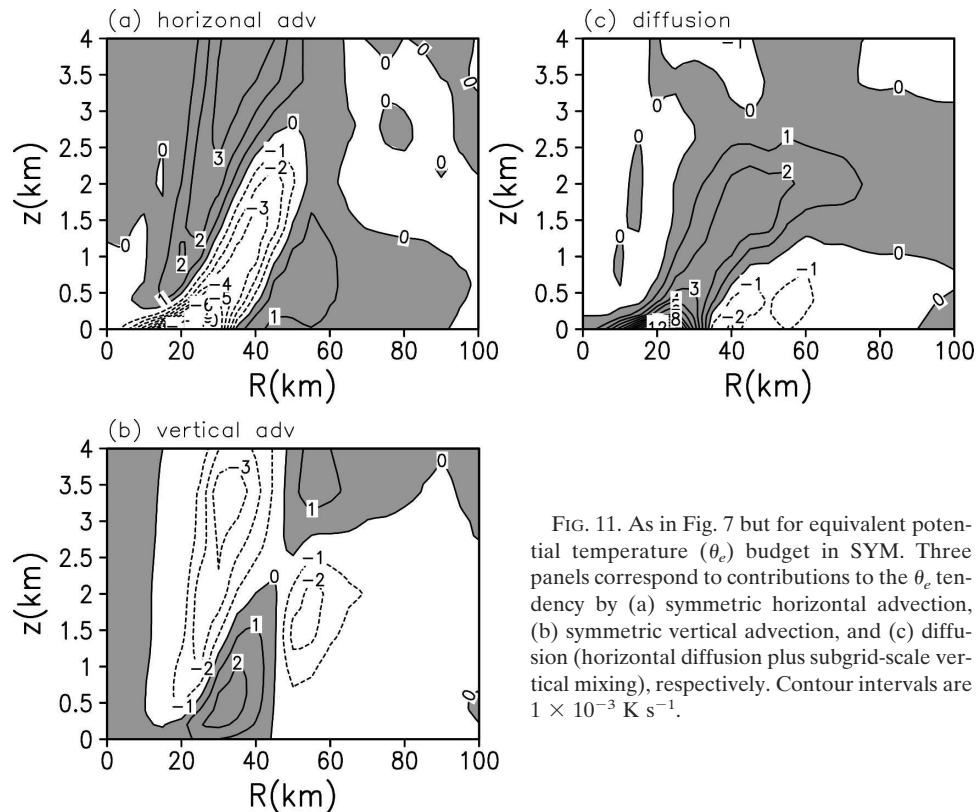


FIG. 11. As in Fig. 7 but for equivalent potential temperature (θ_e) budget in SYM. Three panels correspond to contributions to the θ_e tendency by (a) symmetric horizontal advection, (b) symmetric vertical advection, and (c) diffusion (horizontal diffusion plus subgrid-scale vertical mixing), respectively. Contour intervals are $1 \times 10^{-3} \text{ K s}^{-1}$.

mid-upper troposphere and reducing the outward eyewall tilt in CTL. For both 3D and axisymmetric runs, the θ_e budget in the boundary layer near the RMW is dominated by the surface enthalpy flux and radial cold advection of θ_e . However, in the axisymmetric simulation, the downdrafts across the top of the boundary layer just outside the eyewall play an essential role in importing low θ_e air into the subcloud layer and maintaining a large entropy deficit at the air–sea interface near the RMW. This mechanism is much weaker in the 3D simulation, in which the boundary layer θ_e is higher, and the entropy deficit at the air–sea interface is smaller, resulting in less energy input from the ocean and limiting the maximum intensity. Further, consistent with Persing and Montgomery (2003), we also found that the entrained high θ_e from the eye to the eyewall by the parameterized mixing represents an additional source of energy input and can thus lead to a superintense storm. This parameterized mixing (entrainment) is affected considerably by the storm structure and energy input from the ocean, both are modified by the 3D asymmetric eddies in the 3D simulation. The resolved 3D eddies themselves also directly contribute negatively to the θ_e budget in the eyewall and thus weakens the storm.

b. Discussion

Many theories related to the intensity of TCs, such as the maximum potential intensity, have been based on the assumption that TCs are axisymmetric. In reality, however, a TC is a highly rotating warm-cored vortex with considerable asymmetric structure. Although increasing attention has been given to the dynamics of the asymmetric structure in recent years, our understanding of TCs is still largely limited to the axisymmetric dynamics. Therefore, a natural question arises with regard to the importance of the asymmetric structure to TC dynamics. This question is difficult to address with observations of real TCs since all TCs in nature have asymmetries. Numerical experiments are relatively easy to control and can provide some hints. Thus, we conducted a comparative numerical study of TCs simulated in a 3D model and in its axisymmetric version.

As far as we know, there is no detailed comparison between the simulated TCs in 3D and axisymmetric 2D models so far, however, studies comparing the simulation of convection in 3D and symmetric 2D models in Cartesian coordinates have been reported (e.g., Tompkins 2000; Moeng et al. 1996, 2004). Moeng et al. (1996) investigated the impact of dimensionality on modeled

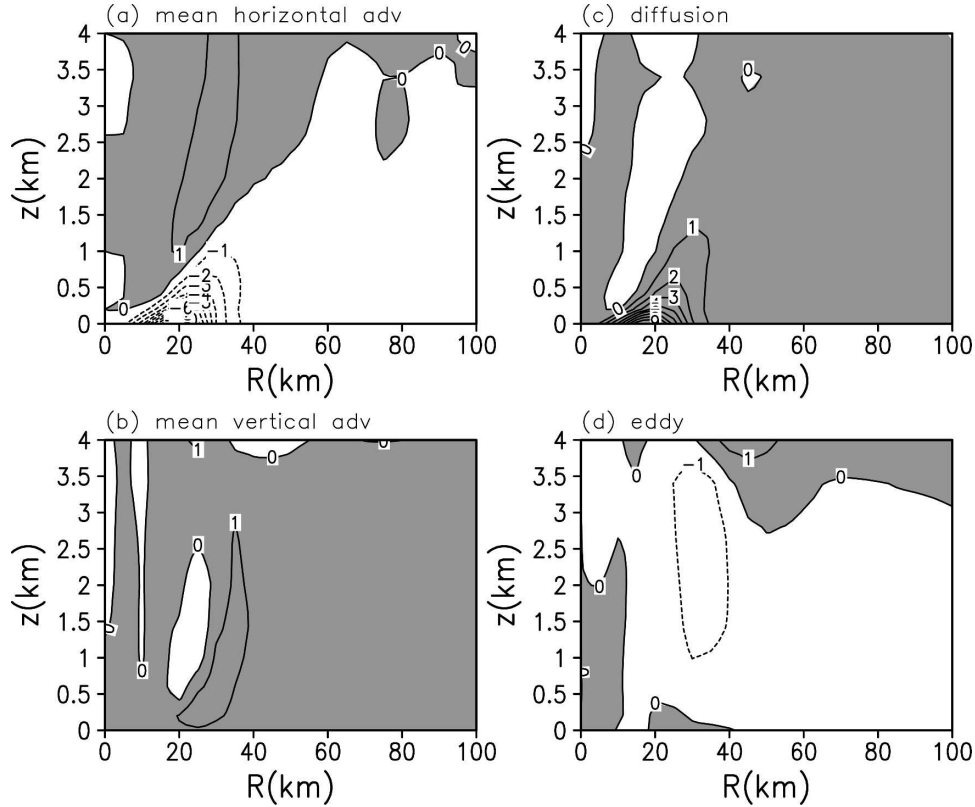


FIG. 12. As in Fig. 11 but for CTL. Four panels correspond to contributions to the azimuthal mean θ_e tendency by (a) symmetric (mean) horizontal advection, (b) symmetric (mean) vertical advection, (c) diffusion, and (d) asymmetric eddies (eddy). Contour intervals are $1 \times 10^{-3} \text{ K s}^{-1}$.

atmospheric convection occurring in the planetary boundary layer and found that 2D simulations were useful for studying the overall evolution of the mean and scalar flux profiles despite the obvious eddy structure differences in 2D and 3D. However, recently Moeng et al. (2004) showed that turbulent kinetic energy, surface friction velocity, and velocity variances were sensitive to the subgrid horizontal diffusion in the model. With the tuned subgrid horizontal diffusion coefficient, the model could generate hypothetical 2D plumes that behaved somewhat like their 3D counterparts. They found that a proper amount of horizontal diffusion was needed to accomplish sufficient dissipation that could not otherwise occur within 2D nonlinear dynamics.

Since our strategy in this study was to compare 2D and 3D simulations with identical model parameters except for the geometry, we also faced the possibility of different formulations of horizontal diffusion and their impact on the TC intensity. This possibility was ruled out in our study by two additional runs. One is an additional 3D run, in which the deformation is calculated according to Eq. (5) using azimuthally averaged flow.

The other is an additional symmetric run, in which the horizontal diffusion was calculated in the Cartesian coordinates, in the same way as in the 3D run. As an example, we show in Figs. 14 and 15 the relative angular momentum budget for the additional axisymmetric run and the additional 3D run, respectively. It can be seen that the overall angular momentum budget of the additional symmetric run (the additional 3D run) is quite similar to that in the SYM (CTL) run given in Fig. 7 (Fig. 8). Therefore, our findings appear to be robust and unaffected by the calculation of deformation-based horizontal diffusion.

A mature TC is characterized by two-dimensional highly organized convection and strong mean tangential circulation, which is very different from the randomly occurring convection observed in a low-wind environment. This may explain why many features of a TC can be understood based on the axisymmetric assumption. However, the axisymmetric model puts an unrealistic restriction on the freedom of turbulence processes. Namely, it is impossible to produce 3D turbulence within a 2D model. This is an inevitable outcome of using an axisymmetric model. Certain impacts

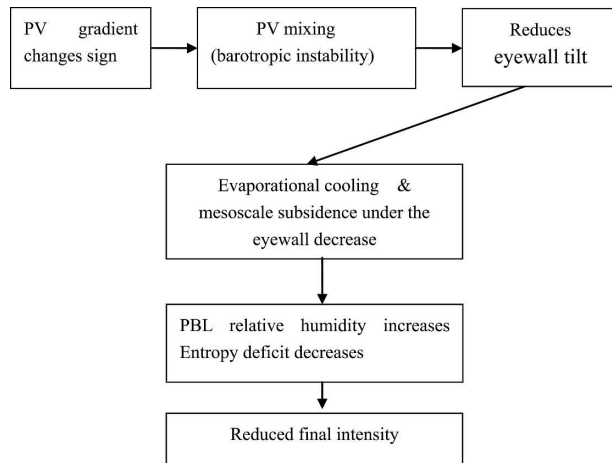


FIG. 13. Schematic diagram showing how the asymmetric eddies reduce the outward eyewall tilt, modifying the air-sea entropy deficit under the eyewall and thus limiting the TC intensity in the 3D simulation. See text for details.

of this freedom reduction can be identified in our results. For example, the contribution by parameterized horizontal diffusion to the azimuthal mean angular momentum in CTL is considerably smaller than its coun-

terpart in SYM. The additional experiment using the symmetric deformation operator in the 3D model gives similar results, suggesting that it is the difference in the deformation structure of simulated 2D and 3D TCs, rather than the deformation operator itself, that determines the different magnitudes in the parameterized horizontal diffusion. Nevertheless, given finest resolution of 5km and the specified subgrid-scale eddy viscosity parameters used in this paper, in the azimuthal mean angular momentum budget, the sum of the contributions by parameterized horizontal diffusion and explicit eddy mixing in CTL is approximately equal to the contribution by parameterized horizontal diffusion in SYM alone, indicating that the symmetric model can largely represents the unresolved (such as the 3D eddies) turbulent process similar to its 3D counterpart. However, this is realized at the expense of TC structure changes. In particular, the larger parameterized horizontal diffusion in 2D run requires a sharper gradient of tangential wind near RMW than its counterpart in 3D run. Therefore caution should be paid to the interpretation of the TC structure obtained in the symmetric model in view of the fact that any TC in the real world resides in a 3D space.

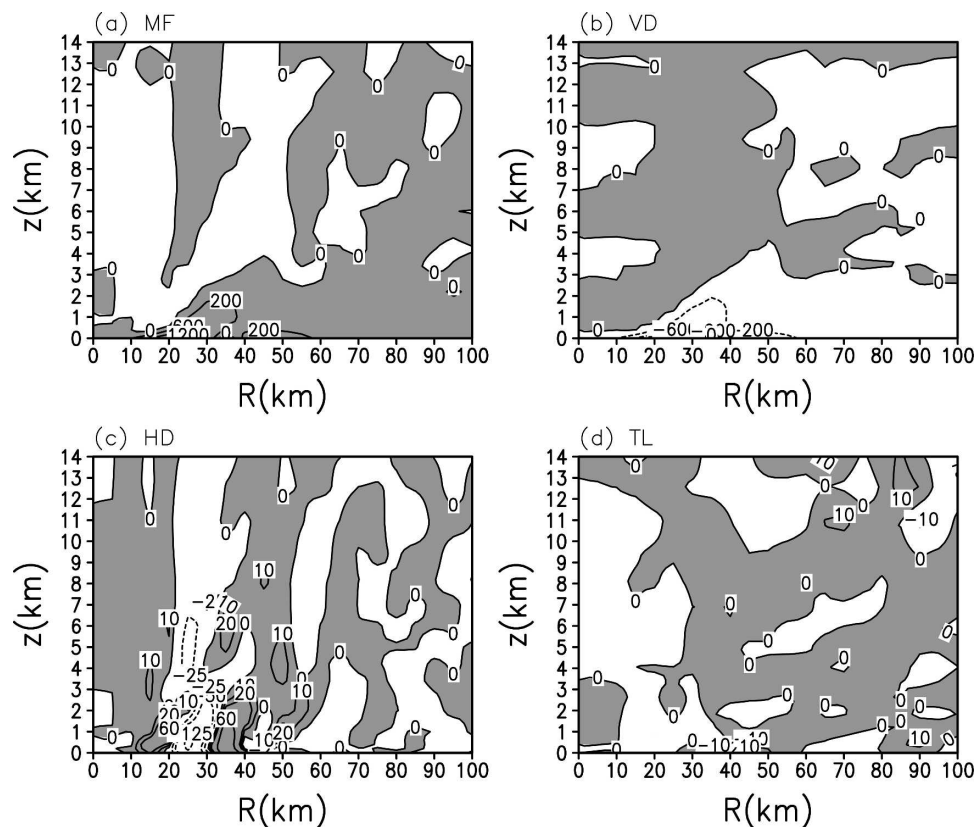


FIG. 14. As in Fig. 7 but for the additional symmetric run.

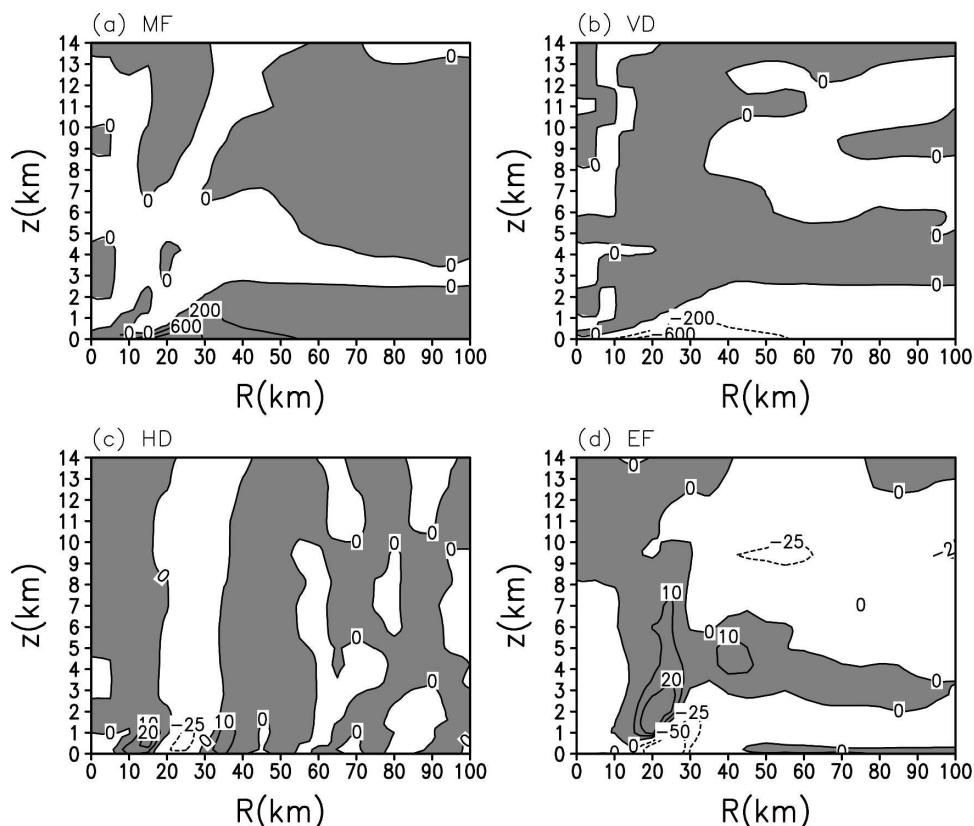


FIG. 15. As in Fig. 8 but for the additional 3D run.

Since a direct interpretation in terms of the angular momentum budget can hardly separate the cause and effect, the angular momentum budget is not ideal for explaining the intensity difference at mature stage. Specifically, the direct spindown by eddies does not inevitably lead to a weaker TC since it is possible that both asymmetric and symmetric circulations become stronger as long as more energy can be extracted from the ocean. Therefore a pure dynamical consideration is insufficient to explain the intensity difference in the simulated storms in the 2D and 3D runs. We have provided an alternative that explains the difference from an energetic viewpoint.

Finally, this work should be considered as an initial step toward a detailed understanding of the effect of inner-core convective asymmetries on TC intensity. Our findings are yet to be verified with higher-resolution nonhydrostatic simulations and to be extended to include the effect of externally forced convective asymmetries.

Acknowledgments. The authors are grateful to Dr. Gisela Speidel and Mr. Thomas Dunn for their careful reading and editing of the manuscript. Special thanks

also go to Prof. Kerry Emanuel for providing easily accessible code for his PI calculations. Comments from Prof. Kerry Emanuel, Prof. Michael Montgomery, Prof. Thomas Schroeder, Dr. John Persing, and two anonymous reviewers helped improve the manuscript. This study has been supported by ONR Grant N000-14-02-1-0532 and NSF Grant ATM-0427128. Additional support has been provided by the JMSTEC through its sponsorship of the International Pacific Research Center (IPRC) in the School of Ocean and Earth Science and Technology (SOEST) at the University of Hawaii.

APPENDIX A

Numerical Treatment for Horizontal Diffusion

A fourth-order horizontal diffusion scheme is adopted in the numerical integration in cylindrical coordinates. For any given variable S (S can be U , V , T , etc.)

$$D_s = -K_H \nabla^4 s. \quad (\text{A1})$$

Following Bird et al. (1960, p. 739), for vector variables, we have

$$\nabla^2 U_j = 2 \left(\frac{U_{j+1} + U_{j-1} - 2U_j}{d^2} + \frac{1}{r_j} \frac{U_{j+1} - U_{j-1}}{2d} - \frac{U_j}{r_j^2} \right) \quad (\text{A2})$$

$$\nabla^2 V_j = \left(\frac{V_{j+1} + V_{j-1} - 2V_j}{d^2} + \frac{1}{r_j} \frac{V_{j+1} - V_{j-1}}{2d} - \frac{V_j}{r_j^2} \right). \quad (\text{A3})$$

Then

$$\begin{aligned} \nabla^4 U_j &= 2 \left(\frac{\nabla^2 U_{j+1} + \nabla^2 U_{j-1} - 2\nabla^2 U_j}{d^2} + \frac{1}{r_j} \frac{\nabla^2 U_{j+1} - \nabla^2 U_{j-1}}{2d} - \frac{\nabla^2 U_j}{r_j^2} \right) \\ &= \frac{4}{d^2} \left[\frac{U_{j+2} - 4U_{j+1} + 6U_j - 4U_{j-1} + U_{j-2}}{d^2} + \left(\frac{1}{r_{j+1}} \frac{U_{j+2} - U_j}{2d} + \frac{1}{r_{j-1}} \frac{U_j - U_{j-2}}{2d} - \frac{2}{r_j} \frac{U_{j+1} - U_{j-1}}{2d} \right) \right. \\ &\quad \left. - \left(\frac{U_{j+1}}{r_{j+1}^2} + \frac{U_{j-1}}{r_{j-1}^2} - \frac{2U_j}{r_j^2} \right) \right] + \frac{4}{r_j 2d} \left[\frac{U_{j+2} - 2U_{j+1} + 2U_{j-1} - U_{j-2}}{d^2} + \left(\frac{1}{r_{j+1}} \frac{U_{j+2} - U_j}{2d} - \frac{1}{r_{j-1}} \frac{U_j - U_{j-2}}{2d} \right) \right. \\ &\quad \left. - \left(\frac{U_{j+1}}{r_{j+1}^2} - \frac{U_{j-1}}{r_{j-1}^2} \right) \right] - \frac{4}{r_j^2} \left(\frac{U_{j+1} + U_{j-1} - 2U_j}{d^2} + \frac{1}{r_j} \frac{U_{j+1} - U_{j-1}}{2d} - \frac{U_j}{r_j^2} \right), \end{aligned} \quad (\text{A4})$$

where j is the index of grip point accounted from the center outward in cylindrical coordinates. Similarly,

$$\begin{aligned} \nabla^4 V_j &= \frac{\nabla^2 V_{j+1} + \nabla^2 V_{j-1} - 2\nabla^2 V_j}{d^2} + \frac{1}{r_j} \frac{\nabla^2 V_{j+1} - \nabla^2 V_{j-1}}{2d} - \frac{\nabla^2 V_j}{r_j^2} \\ &= \frac{1}{d^2} \left[\frac{V_{j+2} - 4V_{j+1} + 6V_j - 4V_{j-1} + V_{j-2}}{d^2} + \left(\frac{1}{r_{j+1}} \frac{V_{j+2} - V_j}{2d} + \frac{1}{r_{j-1}} \frac{V_j - V_{j-2}}{2d} - \frac{2}{r_j} \frac{V_{j+1} - V_{j-1}}{2d} \right) \right. \\ &\quad \left. - \left(\frac{V_{j+1}}{r_{j+1}^2} + \frac{V_{j-1}}{r_{j-1}^2} - \frac{2V_j}{r_j^2} \right) \right] + \frac{1}{r_j 2d} \left[\frac{V_{j+2} - 2V_{j+1} + 2V_{j-1} - V_{j-2}}{d^2} + \left(\frac{1}{r_{j+1}} \frac{V_{j+2} - V_j}{2d} - \frac{1}{r_{j-1}} \frac{V_j - V_{j-2}}{2d} \right) \right. \\ &\quad \left. - \left(\frac{V_{j+1}}{r_{j+1}^2} - \frac{V_{j-1}}{r_{j-1}^2} \right) \right] - \frac{1}{r_j^2} \left(\frac{V_{j+1} + V_{j-1} - 2V_j}{d^2} + \frac{1}{r_j} \frac{V_{j+1} - V_{j-1}}{2d} - \frac{V_j}{r_j^2} \right). \end{aligned} \quad (\text{A5})$$

For any given scalar variable X , we have the following finite differencing operators

$$\nabla^2 X_j = \frac{X_{j+1} + X_{j-1} - 2X_j}{d^2} + \frac{1}{r_j} \frac{X_{j+1} - X_{j-1}}{2d} \quad (\text{A6})$$

$$\begin{aligned} \nabla^4 X_j &= \frac{\nabla^2 X_{j+1} + \nabla^2 X_{j-1} - 2\nabla^2 X_j}{d^2} + \frac{1}{r_j} \frac{\nabla^2 X_{j+1} - \nabla^2 X_{j-1}}{2d} \\ &= \frac{1}{d^2} \left[\frac{X_{j+2} - 4X_{j+1} + 6X_j - 4X_{j-1} + X_{j-2}}{d^2} + \left(\frac{1}{r_{j+1}} \frac{X_{j+2} - X_j}{2d} + \frac{1}{r_{j-1}} \frac{X_j - X_{j-2}}{2d} - \frac{2}{r_j} \frac{X_{j+1} - X_{j-1}}{2d} \right) \right] \\ &\quad + \frac{1}{r_j 2d} \left[\frac{X_{j+2} - 2X_{j+1} + 2X_{j-1} - X_{j-2}}{d^2} + \left(\frac{1}{r_{j+1}} \frac{X_{j+2} - X_j}{2d} - \frac{1}{r_{j-1}} \frac{X_j - X_{j-2}}{2d} \right) \right]. \end{aligned} \quad (\text{A7})$$

For the inner boundary at the TC center ($j = 1$), we have

$$\begin{aligned} \nabla^2 U_1 &= 0, \nabla^2 V_1 = 0 \\ \nabla^4 U_1 &= 0, \nabla^4 V_1 = 0. \end{aligned} \quad (\text{A8})$$

$$\nabla^2 X_1 = \frac{X_2 + X_2 - 2X_1}{d^2} = \frac{2(X_2 - X_1)}{d^2} \quad (\text{A9})$$

$$\begin{aligned}\nabla^4 X_1 &= \nabla^2(\nabla^2 X_1) = \frac{2(\nabla^2 X_2 - \nabla^2 X_1)}{d^2} \\ &= \frac{3X_3 - 8X_2 + 5X_1}{d^4}.\end{aligned}\quad (\text{A10})$$

For $j = 2$,

$$\begin{aligned}\nabla^4 U_2 &= 2\left(\frac{\nabla^2 U_3 + \nabla^2 U_1 - 2\nabla^2 U_2}{d^2}\right. \\ &\quad \left.+ \frac{1}{r_2} \frac{\nabla^2 U_3 - \nabla^2 U_1}{2d} - \frac{\nabla^2 U_2}{r_2^2}\right) \\ &= 2\left(\frac{\nabla^2 U_3 - 2\nabla^2 U_2}{d^2} + \frac{1}{r_2} \frac{\nabla^2 U_3}{2d} - \frac{\nabla^2 U_2}{r_2^2}\right)\end{aligned}\quad (\text{A11})$$

$$\begin{aligned}\nabla^4 V_2 &= \frac{\nabla^2 V_3 + \nabla^2 V_1 - 2\nabla^2 V_2}{d^2} \\ &\quad + \frac{1}{r_2} \frac{\nabla^2 V_3 - \nabla^2 V_1}{2d} - \frac{\nabla^2 V_2}{r_2^2} \\ &= \frac{\nabla^2 V_3 - 2\nabla^2 V_2}{d^2} + \frac{1}{r_2} \frac{\nabla^2 V_3}{2d} - \frac{\nabla^2 V_2}{r_2^2}.\end{aligned}\quad (\text{A12})$$

For any scalar variable,

$$\nabla^4 X_2 = \frac{\nabla^2 X_3 + \nabla^2 X_1 - 2\nabla^2 X_2}{d^2} + \frac{1}{r_2} \frac{\nabla^2 X_3 - \nabla^2 X_1}{2d}.\quad (\text{A13})$$

APPENDIX B

Equations for Budget Analyses

a. Angular momentum budget

The tendency equation for the azimuthal mean relative angular momentum (RAM) in advective form in σ coordinates, $\sigma = p/p_s$, can be written as

$$\begin{aligned}\frac{\partial(r\bar{V})}{\partial t} &= \left(-\bar{U} \frac{\partial r\bar{V}}{\partial r} - \bar{\sigma} \frac{\partial r\bar{V}}{\partial \sigma} - \bar{U}\bar{V} - f\bar{r}\bar{U}\right) \\ &\quad + \left(-\overline{U' \frac{\partial rV'}{\partial r}} - \overline{\sigma' \frac{\partial rV'}{\partial \sigma}} - \overline{U'V'}\right) \\ &\quad + r\bar{D}_\lambda + r\bar{F}_\lambda,\end{aligned}\quad (\text{B1})$$

where t , r , λ , p , and p_s are the time, radius, azimuth, pressure, and surface pressure; \bar{U} , \bar{V} and U' , V' are the symmetric and asymmetric radial and tangential winds, respectively; \bar{D}_λ and \bar{F}_λ are the horizontal and vertical diffusions of the azimuthal mean RAM. In the analysis

the origin of the cylindrical coordinates is placed at the surface pressure minimum. Terms on the rhs of (B1) are, respectively, contributions by symmetric (mean) flow advection (MF); eddy flow advection (EF); horizontal diffusion (HD) and vertical diffusion (VD).

b. PV budget

Following Hoskins et al. (1985), the PV in sigma and cylindrical coordinates can be written as

$$P = -g\zeta_a \cdot \nabla_3 \theta = -g(f\mathbf{k} + \nabla_3 \times \mathbf{V}) \cdot \nabla_3 \theta \quad (\text{B2})$$

$$\mathbf{V} = U\mathbf{r} + V\boldsymbol{\lambda} \quad \nabla_3 = U\mathbf{r} + V\boldsymbol{\lambda} - \dot{\sigma}\mathbf{k} \quad (\text{B3})$$

$$\nabla_3 = \mathbf{r} \frac{\partial}{\partial r} + \boldsymbol{\lambda} \frac{\partial}{r\partial \lambda} - \mathbf{k} \frac{\partial}{\partial \sigma}, \quad (\text{B4})$$

where ζ_a is the three-dimensional vorticity vector, U and V are the radial and azimuthal winds, respectively, \mathbf{k} is the unit vector in the vertical with positive upward, and \mathbf{r} , $\boldsymbol{\lambda}$ are unit vectors in the radial and azimuthal directions, respectively.

The PV tendency equation can be written (Wu and Wang 2001) as

$$\begin{aligned}\frac{\partial(p_s P)}{\partial t} &= -\nabla_3 \cdot (\nabla_3 p_s P) - g\nabla_3 \cdot \left(-\frac{Q}{\pi} \zeta_a\right) \\ &\quad - g\nabla_3 \cdot (\nabla \theta \times \mathbf{F}).\end{aligned}\quad (\text{B5})$$

Here diabatic heating (Q , in K s^{-1}) includes condensational heating, horizontal, and vertical temperature diffusion, and dissipative heating, while both the horizontal and vertical diffusions (surface friction included in the latter) of momentum are grouped in \mathbf{F} .

Separating the basic quantities into the azimuthal mean and the deviation from the mean (eddy) components, and averaging Eq. (B5) along the azimuthal direction, we have

$$\begin{aligned}\frac{\partial(p_s \bar{P})}{\partial t} &= -\nabla_2 \cdot (\bar{\nabla}_3 p_s \bar{P}) - g\nabla_2 \cdot \left(-\frac{\bar{Q}}{\pi} \bar{\zeta}_a\right) \\ &\quad - g\nabla_2 \cdot (\nabla_3 \bar{\theta} \times \bar{\mathbf{F}}) - \nabla_2 \\ &\quad \cdot \left(p_s \overline{\nabla'_3 P'} - g \frac{\overline{Q' \zeta'_a}}{\pi} + g \overline{\nabla'_3 \theta'} \times \bar{\mathbf{F}}'\right),\end{aligned}\quad (\text{B6})$$

where terms on the rhs of Eq. (B6) are contributions to the azimuthal mean PV budget by symmetric (mean) motion; symmetric (mean) diabatic heating; symmetric (mean) diffusion; and asymmetric eddies, respectively.

c. θ_e budget

As discussed in Klemp and Wilhelmson (1978) and Rotunno and Emanuel (1987), θ_e is not precisely conserved in the model. Following the method introduced by Rotunno and Emanuel (1987), the tendency equation for θ_e can be written as

$$\frac{\partial \theta_e}{\partial t} = -\mathbf{V}_3 \cdot \nabla_3 \theta_e + D_{\theta_e} + F_{\theta_e} + H_{\theta_e}, \quad (\text{B7})$$

where F_{θ_e} , D_{θ_e} , and H_{θ_e} are the contributions by subgrid-scale vertical mixing, horizontal diffusion, and dissipative heating, respectively. To be consistent with model calculations, we use the following forms in our budget analysis.

$$\frac{\partial \theta_e}{\partial t} \approx \frac{\partial \theta}{\partial t} + \frac{L}{C_p \pi} \frac{\partial q_v}{\partial t} \quad (\text{B8})$$

$$\mathbf{V}_3 \cdot \nabla \theta_e \approx \mathbf{V}_3 \cdot \nabla \theta + \frac{L}{C_p \pi} \mathbf{V}_3 \cdot \nabla q_v \quad (\text{B9})$$

$$D_{\theta_e} \approx \frac{1}{\pi} D_T + \frac{L}{C_p \pi} D_{q_v} \quad (\text{B10})$$

$$F_{\theta_e} \approx \frac{1}{\pi} F_T + \frac{L}{C_p \pi} F_{q_v} \quad (\text{B11})$$

$$H_{\theta_e} \approx \frac{1}{\pi} H_T, \quad (\text{B12})$$

where D_T , F_T , H_T , and D_{q_v} , F_{q_v} are contributions to temperature tendency by horizontal diffusion, vertical mixing, dissipative heating, and contributions to the water vapor tendency by horizontal diffusion and vertical mixing, respectively.

Separating the basic quantities into an azimuthal mean and the deviation (eddy) from the azimuthal mean components, and averaging the equation along the azimuthal direction, we obtain

$$\frac{\partial \bar{\theta}_e}{\partial t} = \text{MHADV} + \text{MVADV} + \text{EDDY} + \text{DISS}, \quad (\text{B13})$$

where

$$\text{MHADV} = -\bar{U} \frac{\partial \bar{\theta}}{\partial r} - \bar{U} \frac{L}{C_p \pi} \frac{\partial \bar{q}_v}{\partial r} \quad (\text{B14})$$

$$\text{MVADV} = -\bar{\sigma} \frac{\partial \bar{\theta}}{\partial \sigma} - \bar{\sigma} \frac{L}{C_p \pi} \frac{\partial \bar{q}_v}{\partial \sigma} \quad (\text{B15})$$

$$\begin{aligned} \text{EDDY} = & -\overline{U' \frac{\partial \theta'}{\partial r}} - \frac{L}{C_p \pi} \overline{U' \frac{\partial q'_v}{\partial r}} - \overline{V' \frac{\partial \theta'}{r \partial \lambda}} \\ & - \frac{L}{C_p \pi} \overline{V' \frac{\partial q'_v}{r \partial \lambda}} - \overline{\sigma' \frac{\partial \theta'}{\partial \sigma}} - \frac{L}{C_p \pi} \overline{\sigma' \frac{\partial q'_v}{\partial \sigma}} \end{aligned} \quad (\text{B16})$$

$$\begin{aligned} \text{DISS} = & \frac{1}{\pi} \overline{F_T} + \frac{L}{C_p \pi} \overline{F_{q_v}} + \frac{1}{\pi} \overline{D_T} + \frac{L}{C_p \pi} \overline{D_{q_v}} \\ & + \frac{1}{\pi} \overline{H_T}. \end{aligned} \quad (\text{B17})$$

The four terms on the rhs in Eq. (B13) represent contributions to the azimuthal mean θ_e budget by radial and vertical advection of azimuthal mean θ_e by the azimuthal mean (symmetric) flow, eddy processes, and all diabatic processes including subgrid-scale vertical mixing and horizontal diffusion, and dissipative heating.

REFERENCES

- Barnes, G. M., E. J. Zipser, D. P. Jorgensen, and F. D. Marks Jr., 1983: Mesoscale and convective structure of a hurricane rainband. *J. Atmos. Sci.*, **40**, 2125–2137.
- Bender, M. A., 1997: The effect of relative flow on the asymmetric structure in the interior of hurricanes. *J. Atmos. Sci.*, **54**, 703–724.
- Bird, R. B., W. E. Schubert, and E. N. Lightfoot, 1960: *Transport Phenomena*. Wiley & Sons, 780 pp.
- Bister, M., and K. Emanuel, 1998: Dissipative heating and hurricane intensity. *Meteor. Atmos. Phys.*, **65**, 223–240.
- , and —, 2002a: Low frequency variability of tropical cyclone potential intensity. 1. Interannual to interdecadal variability. *J. Geophys. Res.*, **107**, 48011, doi:10.1029/2001JD000776.
- , and —, 2002b: Low frequency variability of tropical cyclone potential intensity. 2. Climatology for 1982–1995. *J. Geophys. Res.*, **107**, 4621, doi:10.1029/2001JD000780.
- Black, P. G., and F. D. Marks Jr., 1991: The structure of an eye-wall meso-vortex in Hurricane Hugo (1989). Preprints, *19th Conf. on Hurricanes and Tropical Meteorology*, Miami, FL, Amer. Meteor. Soc., 579–582.
- Camp, J. P., and M. T. Montgomery, 2001: Hurricane maximum intensity: Past and present. *Mon. Wea. Rev.*, **129**, 1704–1717.
- Chen, Y., and M. K. Yau, 2001: Spiral bands in a simulated hurricane. Part I: Vortex Rossby wave verification. *J. Atmos. Sci.*, **58**, 2128–2145.
- Dengler, K., and D. Keyser, 2000: Intensification of tropical cyclone-like vortices in uniform zonal background flow. *Quart. J. Roy. Meteor. Soc.*, **126**, 549–568.
- Emanuel, K., 1986: An air–sea interaction theory for tropical cyclones. I: Steady-state maintenance. *J. Atmos. Sci.*, **43**, 585–604.
- , 1988: The maximum intensity of hurricanes. *J. Atmos. Sci.*, **45**, 1143–1155.
- , 1989: The finite-amplitude nature of tropical cyclogenesis. *J. Atmos. Sci.*, **46**, 3431–3456.
- , 1995: Sensitivity of tropical cyclones to surface exchange coefficients and a revised steady-state model incorporating eye dynamics. *J. Atmos. Sci.*, **52**, 3969–3976.

- , 1997: Some aspects of hurricane inner core dynamics and energetics. *J. Atmos. Sci.*, **54**, 1014–1026.
- Frank, W. M., and E. A. Ritchie, 1999: Effects of environmental flow upon tropical cyclone structure. *Mon. Wea. Rev.*, **127**, 2044–2061.
- , and —, 2001: Effects of vertical wind shear on the intensity and structure of numerically simulated hurricanes. *Mon. Wea. Rev.*, **129**, 2249–2269.
- Gray, W. M., 1968: Global view of the origin of tropical disturbances and storms. *Mon. Wea. Rev.*, **96**, 669–700.
- , E. Ruprecht, and R. Phelps, 1975: Relative humidity in tropical weather systems. *Mon. Wea. Rev.*, **103**, 685–690.
- Guinn, T. A., and W. H. Schubert, 1993: Hurricane spiral bands. *J. Atmos. Sci.*, **50**, 3380–3404.
- Heymsfield, G. M., J. B. Halverson, J. Simpson, L. Tian, and T. P. Bui, 2001: ER-2 Doppler radar investigations of the eyewall of Hurricane Bonnie during the Convection and Moisture Experiment-3. *J. Appl. Meteor.*, **40**, 1310–1330.
- Holland, G. J., 1997: The maximum potential intensity of tropical cyclones. *J. Atmos. Sci.*, **54**, 2519–2541.
- Hoskins, B. J., M. E. McIntyre, and A. W. Robertson, 1985: On the use and significance of isentropic potential vorticity maps. *Quart. J. Roy. Meteor. Soc.*, **111**, 877–946.
- Jacob, S. D., L. K. Shay, A. J. Mariano, and P. G. Black, 2000: The 3D oceanic mixed layer response to Hurricane Gilbert. *J. Phys. Oceanogr.*, **30**, 1407–1429.
- Klemp, J. B., and R. B. Wilhelmson, 1978: The simulation of three-dimensional convective storm dynamics. *J. Atmos. Sci.*, **35**, 1070–1096.
- Kossin, J. P., B. D. McNoldy, and W. H. Schubert, 2002: Vortical swirls in hurricane eye clouds. *Mon. Wea. Rev.*, **130**, 3144–3149.
- Lewis, B. M., and H. F. Hawkins, 1982: Polygonal eyewalls and rainbands in hurricanes. *Bull. Amer. Meteor. Soc.*, **63**, 1294–1301.
- Li, X., and B. Wang, 1996: Acceleration of the hurricane beta drift by shear strain rate of an environmental flow. *J. Atmos. Sci.*, **53**, 327–334.
- Liu, Y., D.-L. Zhang, and M. K. Yau, 1999: A multiscale numerical study of Hurricane Andrew (1992). Part II: Kinematics and inner-core structures. *Mon. Wea. Rev.*, **127**, 2597–2616.
- MacDonald, N. J., 1968: The evidence for the existence of Rossby-like waves in the hurricane vortex. *Tellus*, **20**, 138–150.
- Moeng, C.-H., and Coauthors, 1996: Simulation of a stratocumulus-topped planetary boundary layer: Intercomparison among different numerical codes. *Bull. Amer. Meteor. Soc.*, **77**, 261–278.
- , J. C. McWilliams, R. Rotunno, P. P. Sullivan, and J. Weil, 2004: Investigating 2D modeling of atmospheric convection in the PBL. *J. Atmos. Sci.*, **61**, 889–903.
- Möller, J. D., and M. T. Montgomery, 1999: Vortex Rossby waves and hurricane intensification in a barotropic model. *J. Atmos. Sci.*, **56**, 1674–1687.
- , and —, 2000: Tropical cyclone evolution via potential vorticity anomalies in a three-dimensional balance model. *J. Atmos. Sci.*, **57**, 3366–3387.
- Montgomery, M. T., and R. J. Kallenbach, 1997: A theory for vortex Rossby waves and its application to spiral bands and intensity changes in hurricanes. *Quart. J. Roy. Meteor. Soc.*, **123**, 435–465.
- , and J. Enagonio, 1998: Tropical cyclogenesis via convectively forced vortex Rossby waves in a three-dimensional quasigeostrophic model. *J. Atmos. Sci.*, **55**, 3176–3207.
- , V. A. Vladimirov, and P. V. Denissenko, 2002: An experimental study on hurricane mesovortices. *J. Fluid Mech.*, **471**, 1–32.
- Nolan, D. S., and M. T. Montgomery, 2002: Nonhydrostatic, three-dimensional perturbations to balanced, hurricane-like vortices. Part I: Linearized formulation, stability, and evolution. *J. Atmos. Sci.*, **59**, 2989–3020.
- Peng, M. S., B. F. Jeng, and R. T. Williams, 1999: A numerical study on tropical cyclone intensification. Part I: Beta effect and mean flow effect. *J. Atmos. Sci.*, **56**, 1404–1423.
- Persing, J., and M. T. Montgomery, 2003: Hurricane superintensity. *J. Atmos. Sci.*, **60**, 2349–2371.
- Powell, M. D., 1990a: Boundary layer structure and dynamics in outer hurricane rainbands. Part I: Mesoscale rainfall and kinematic structure. *Mon. Wea. Rev.*, **118**, 891–917.
- , 1990b: Boundary layer structure and dynamics in outer hurricane rainbands. Part II: Downdraft modification and mixed layer recovery. *Mon. Wea. Rev.*, **118**, 918–938.
- Rotunno, R., and K. Emanuel, 1987: An air–sea interaction theory for tropical cyclones. Part II: Evolutionary study using a non-hydrostatic axisymmetric model. *J. Atmos. Sci.*, **44**, 542–561.
- Schubert, W. H., M. T. Montgomery, R. K. Taft, T. A. Guinn, S. R. Fulton, J. P. Kossin, and J. P. Edwards, 1999: Polygonal eyewalls, asymmetric eye contraction, and potential vorticity mixing in hurricanes. *J. Atmos. Sci.*, **56**, 1197–1223.
- Shapiro, L. J., 1983: The asymmetric boundary layer flow under a translating hurricane. *J. Atmos. Sci.*, **40**, 1984–1998.
- , and M. T. Montgomery, 1993: A three-dimensional balance theory for rapid rotating vortices. *J. Atmos. Sci.*, **50**, 3322–3335.
- Shay, L. K., A. J. Mariano, S. D. Jacob, and E. H. Ryan, 1998: Mean and near-inertial ocean current response to Hurricane Gilbert. *J. Phys. Oceanogr.*, **28**, 858–889.
- Smith, G. B., and M. T. Montgomery, 1995: Vortex axisymmetrization: Dependence on azimuthal wave number or asymmetric radial structure changes. *Quart. J. Roy. Meteor. Soc.*, **121**, 1615–1650.
- Tompkins, A. M., 2000: The impact of dimensionality on long-term cloud-resolving model simulations. *Mon. Wea. Rev.*, **128**, 1521–1535.
- Wang, Y., 1999: A triply-nested movable mesh tropical cyclone model with explicit cloud microphysics-TCM3. BMRC Rep. 74, Bureau of Meteorology Research Center, Australia, 81 pp.
- , 2001: An explicit simulation of tropical cyclones with a triply nested movable mesh primitive equation model: TCM3. Part I: Model description and control experiment. *Mon. Wea. Rev.*, **129**, 1370–1394.
- , 2002a: Vortex Rossby waves in a numerically simulated tropical cyclone. Part I: Overall structure, potential vorticity, and kinetic energy budgets. *J. Atmos. Sci.*, **59**, 1213–1238.
- , 2002b: Vortex Rossby waves in a numerically simulated tropical cyclone. Part II: The role in tropical cyclone structure and intensity changes. *J. Atmos. Sci.*, **59**, 1239–1262.
- , 2002c: An explicit simulation of tropical cyclones with a triply nested movable mesh primitive equation model: TCM3. Part II: Model refinements and sensitivity to cloud microphysics parameterization. *Mon. Wea. Rev.*, **130**, 3022–3036.
- , and G. J. Holland, 1996a: Beta drift of baroclinic vortices. Part I: Adiabatic vortices. *J. Atmos. Sci.*, **53**, 411–427.
- , and —, 1996b: Beta drift of baroclinic vortices. Part II: Diabatic vortices. *J. Atmos. Sci.*, **53**, 3737–3756.

- , and —, 1996c: Tropical cyclone motion and evolution in vertical shear. *J. Atmos. Sci.*, **53**, 3313–3332.
- , and C.-C. Wu, 2004: Current understanding of tropical cyclone structure and intensity changes—A review. *Meteor. Atmos. Phys.*, **87**, 257–278.
- Willoughby, H. E., and P. G. Blacks, 1996: Hurricane Andres in Florida: Dynamics of a disaster. *Bull. Amer. Meteor. Soc.*, **77**, 543–549.
- , F. D. Marks, and R. J. Feinberg, 1984: Stationary and moving convective bands in hurricanes. *J. Atmos. Sci.*, **41**, 3189–3211.
- Wu, C.-C., 2001: Numerical simulation of Typhoon Gladys (1994) and its interaction with Taiwan terrain using the GFDL hurricane model. *Mon. Wea. Rev.*, **129**, 1533–1549.
- , and Y. Kurihara, 1996: A numerical study of the feedback mechanism of hurricane–environment interaction on hurricane movement from the potential vorticity perspective. *J. Atmos. Sci.*, **53**, 2264–2282.
- , and H.-J. Cheng, 1999: An observational study of environmental influences on the intensity changes of Typhoons Flo (1990) and Gene (1990). *Mon. Wea. Rev.*, **127**, 3003–3031.
- Wu, L., and B. Wang, 2001: Effects of convective heating on movement and vertical coupling of tropical cyclones: A numerical study. *J. Atmos. Sci.*, **58**, 3639–3649.
- , and S. A. Braun, 2004: Effect of convective asymmetries on hurricane intensity: A numerical study. *J. Atmos. Sci.*, **61**, 3065–3081.
- Zhang, D.-L., and E. Altshuler, 1999: The effects of dissipative heating on hurricane intensity. *Mon. Wea. Rev.*, **127**, 3032–3038.
- , and X. Wang, 2003: Dependence of hurricane intensity and structure on vertical resolution and time-step size. *Adv. Atmos. Sci.*, **20**, 711–725.
- Zhu, T., D.-L. Zhang, and F. Weng, 2004: Numerical simulation of Hurricane Bonnie (1998). Part I: Eyewall evolution and intensity changes. *Mon. Wea. Rev.*, **132**, 225–241.